



***B*-fields and Dust in Interstellar Filaments Using Dust Polarization (BALLAD-POL). III. Grain Alignment and Disruption Mechanisms in G34.43+0.24 Using Polarization Observations from JCMT/POL-2**

Saikhom Pravash^{1,2} , Archana Soam¹ , Pham Ngoc Diep^{3,4} , Thiem Hoang^{5,6} , Nguyen Bich Ngoc^{3,4} , and Le Ngoc Tram⁷ 

¹ Indian Institute of Astrophysics, II Block, Koramangala, 560034, India; saikhom.singh@iiap.res.in, spravash11@gmail.com

² Pondicherry University, R.V. Nagar, Kalapet, Puducherry, 605014, India

³ Department of Astrophysics, Vietnam National Space Center, Vietnam Academy of Science and Technology, 18 Hoang Quoc Viet, Hanoi, Vietnam

⁴ Graduate University of Science and Technology, Vietnam Academy of Science and Technology, 18 Hoang Quoc Viet, Hanoi, Vietnam

⁵ Korea Astronomy and Space Science Institute, 776 Daedeokdae-ro, Yuseong-gu, Daejeon 34055, Republic of Korea

⁶ University of Science and Technology, Korea, 217 Gajeong-ro, Yuseong-gu, Daejeon 34113, Republic of Korea

⁷ Leiden Observatory, Leiden University, PO Box 9513, 2300 RA Leiden, The Netherlands

Received 2024 October 22; revised 2025 January 5; accepted 2025 January 20; published 2025 March 4

Abstract

Polarization of starlight and thermal dust emission due to aligned non-spherical grains helps us to trace magnetic field (*B*-field) morphology in molecular clouds and to study grain alignment mechanisms. In this work, we study grain alignment and disruption mechanisms in a filamentary infrared dark cloud G34.43+0.24 using thermal dust polarization observations from JCMT/POL-2 at 850 μm . We study three regions: the North harboring the MM3 core, the Center harboring the MM1 and MM2 cores, and the South harboring no core. We find the decrease in polarization fraction *P* with increasing total intensity and gas column density, known as polarization hole. To disentangle the effect of magnetic field tangling on the polarization hole, we estimate the polarization angle dispersion function. We find depolarizations in the North and Center regions are due to a decrease in the net alignment efficiency of grains, but in the South region, the effect of magnetic field tangling is significant to cause depolarization. To test whether the radiative torque (RAT) mechanism can reproduce the observational data, we calculate minimum alignment and disruption sizes of grains using RAT theory, and our study finds that the RAT alignment (RAT-A) mechanism can explain the depolarizations in the North and Center regions where the *B*-field tangling effect is less important, except for core regions. We find hints of RAT disruption (RAT-D) in the core regions of MM3 in the North, and MM1 and MM2 in the Center. We also find that the high *P* value of around 8%–20% in the outer regions of the filament can potentially be explained by the magnetically enhanced RAT alignment mechanism.

Unified Astronomy Thesaurus concepts: [Interstellar dust \(836\)](#); [Interstellar filaments \(842\)](#); [Star forming regions \(1565\)](#); [Interstellar magnetic fields \(845\)](#)

1. Introduction

Dust grains in the interstellar medium (ISM) have significant influences in various processes, including star and planet formation, gas heating, and cooling and they also provide the surface for the formation of different complex molecules (see B. T. Draine 2003). The polarization of starlight due to dichroic extinction by non-spherical grains aligned with the interstellar magnetic field was first observed by J. S. Hall (1949) and W. A. Hiltner (1949). Such aligned dust grains also reemit polarized thermal emission at longer wavelengths (R. H. Hildebrand 1988). Dust polarization has been widely used to trace the magnetic fields in different environments, from the diffuse ISM to star-forming molecular clouds, and also to study dust properties like shape, size, composition, etc. (e.g., B. T. Draine & B. S. Hensley 2021). Magnetic fields are thought to have a significant impact on the formation and evolution of molecular clouds and on the regulation of star formation processes (see R. M. Crutcher 2012; K. Pattle & L. Fissel 2019). Dust grains are aligned in such a way that their short axes are parallel and long axes are perpendicular to the ambient magnetic field (e.g., A. Lazarian 2007; B. G. Andersson et al. 2015;

A. Lazarian et al. 2015). For the starlight polarization induced by the dichroic extinction by aligned grains, the observed polarization angle provides the plane-of-sky (POS) component of magnetic fields. However, for the polarization of thermal dust emission, the observed polarization angle needs to be rotated by 90° to infer the POS projected magnetic fields (e.g., R. H. Hildebrand 1988).

Recent studies suggest the potential of tracing three-dimensional (3D) magnetic fields using full dust polarization data, including the polarization angle and the polarization fraction (T. Hoang & B. Truong 2024; B. Truong & T. Hoang 2024). This technique relies on the comparison of the observed dust polarization with the accurate model of the dust polarization predicted using the grain alignment physics and dust properties (grain shape and composition). Therefore, it is essential to study in detail the exact physical mechanisms for grain alignment. Several mechanisms for grain alignment have been introduced but many of them are not able to explain fully the observational results (see A. Lazarian 2007 for a review). The most acceptable mechanism that can explain observational results in different environments is radiative torque alignment (RAT-A), first introduced by A. Z. Dolginov & I. G. Mitrofanov (1976) and numerically demonstrated in B. T. Draine & J. C. Weingartner (1997). An analytical radiative torque (RAT) theory was later developed by A. Lazarian & T. Hoang (2007) and T. Hoang & A. Lazarian (2008). According



Original content from this work may be used under the terms of the [Creative Commons Attribution 4.0 licence](#). Any further distribution of this work must maintain attribution to the author(s) and the title of the work, journal citation and DOI.

to RAT-A theory, non-spherical grains exposed to an anisotropic radiation field acquire RATs that tend to spin up grains to suprathermal rotation and align them with the ambient magnetic fields (B. T. Draine & J. C. Weingartner 1997; A. Lazarian & T. Hoang 2007). The efficient alignment of grains is achieved when grains rotate suprathermally with the rotation rate exceeding about three times their thermal angular velocity (T. Hoang & A. Lazarian 2008, 2016). This RAT-A theory predicts an anticorrelation of the polarization fraction P with local gas density and a correlation of P with the radiation field intensity or dust temperature (see H. Lee et al. 2020; T. Hoang et al. 2021). Observations in various regions found a trend of decreasing polarization fraction with the increase in gas column density or total intensity, termed as polarization hole (see, e.g., K. Pattle & L. Fissel 2019; T. Hoang et al. 2021). Various tests of RAT-A in molecular clouds using starlight polarization support the theory well (see review by B. G. Andersson et al. 2015).

However, testing of the RAT-A mechanism in star-forming regions using thermal dust polarization has only recently been conducted (L. N. Tram & T. Hoang 2022; N. B. Ngoc et al. 2023) thanks to the advances in far-IR and submillimeter/millimeter polarimetric instruments HAWC+ (D. A. Harper et al. 2018), POL-2 (P. Friberg et al. 2016), Atacama Large Millimeter/submillimeter Array (ALMA; A. Wootten & A. R. Thompson 2009), NIKA-2 (R. Adam et al. 2018), etc. In the study of dust polarization in different star-forming regions, the polarization hole may be caused not only by a decrease in grain alignment in denser regions as predicted by RAT-A but also by magnetic field fluctuations along the line of sight. Turbulences in the molecular clouds are the main cause of magnetic field fluctuations (T. J. Jones 1989; T. J. Jones et al. 1992; D. Falceta-Gonçalves et al. 2008).

Based on the advance in RAT-A theory, T. Hoang et al. (2019) introduced a new mechanism termed radiative torque disruption (RAT-D). From this RAT-D mechanism, when large grains are irradiated by radiation of very high intensity, they rotate very fast suprathermally as induced by RATs and when the centrifugal stress is greater than the tensile strength of the grains, the large grains could be disrupted into smaller fragments. This RAT-D effect can decrease the polarization fraction when the dust temperature is sufficiently large because of the depletion of large grains (H. Lee et al. 2020) and as RAT-A becomes less effective for smaller grains. Many studies reported that polarization fraction P first increases with dust temperature T_d and when T_d becomes larger, after some T_d value P decreases (e.g., F. P. Santos et al. 2019; Planck Collaboration et al. 2020). This decreasing of P with T_d poses a challenge to the popular RAT-A theory and could be well explained by the RAT-D mechanism. Comprehensive testing of the RAT paradigm (RAT-A and RAT-D) in molecular clouds and interstellar filaments was first studied in L. N. Tram et al. (2021a), N. B. Ngoc et al. (2024), and L. N. Tram et al. (2024). In this paper, we aim to test the RAT paradigm for an infrared dark cloud (IRDC) that contains embedded active star-forming protostellar cores. The decrease in P at larger T_d values can be expected near the high radiation field of protostellar cores in such IRDC due to the RAT-D effect or magnetic field tangling along the line of sight.

IRDCs are usually associated with the formation of mostly high-mass stars and star clusters (J. M. Rathborne et al. 2006) and they contain mostly cold and dense molecular gas. For the study of grain alignment mechanisms, the physical parameters like gas column density or volume density and dust temperature or

equivalently the radiation field strength are crucial. A significant variation of these parameters can favor the study of grain alignment. The filamentary IRDCs show significant variations in these parameters across the filaments from the outer regions toward the inner regions, which makes them ideal regions for studying grain alignment mechanisms. In this work, we study the grain alignment mechanism in the filamentary structured IRDC G34.43+0.24 (hereafter G34) located at a distance of nearly 3.7 kpc (P. Sanhueza et al. 2012; J. B. Foster et al. 2014) and is an active high-mass star-forming cloud (S. Molinari et al. 1998; J. M. Rathborne et al. 2011; T. Sakai et al. 2018). This filament consists of many cores, MM1 to MM9, which are likely at different stages of evolution (H.-R. Chen et al. 2011). The most evolved core MM2 (J. M. Rathborne et al. 2006) is associated with the ultra-compact H II region IRAS 18507+0121 having spectral type B0.5 (S. Molinari et al. 1998; D. S. Shepherd et al. 2004, 2007). MM1 is the brightest millimeter core with hints of high-mass core (J. M. Rathborne et al. 2008) and MM3 hosts a hot corino (T. Yanagida et al. 2014; T. Sakai et al. 2015). We aim to study the grain alignment mechanism over all of the filament, which has significant variations in gas density and dust temperature, by categorizing three regions as North, Center, and South. The central region containing cores MM1 and MM2 is very bright and highly dense as compared to other regions of the filament. The North and Center regions harbor cores but the South region has no cores. This filament is ideal for testing RAT-A and RAT-D because some regions contain embedded sources and some do not. The rest of the paper is organized as follows: Section 2 gives the data acquisition details, Section 3 for the analysis and results, Section 4 presents a discussion of the results and Section 5 gives the summary of the work.

2. Data Acquisition

2.1. Archival Polarization Data

In this work, we use the archival dust polarization data observed by the POL-2 instrument mounted on the James Clerk Maxwell Telescope (JCMT) at $850 \mu\text{m}$. The data is taken from A. Soam et al. (2019). The observations were conducted in 2018 August in band-2 weather conditions using the POL-2 daisy map mode of JCMT. The full width at half-maximum (FWHM) of JCMT/POL-2 at $850 \mu\text{m}$ is $14''.1$. The data were reduced using the STARLINK/SMURF package *pol2map*. The polarization data are debiased using the mean of variances of Q and U to remove statistical bias in the regions of low signal-to-noise ratio (S/N). The debiased polarization fraction and the uncertainty are obtained using Equation (1) for debiased polarization fraction and Equation (2) for the uncertainty in the debiased polarization fraction as given in A. Soam et al. (2019). The selection criteria on the total intensity is kept on $I/\sigma_I > 10$. The quality of the data was checked using different signal-to-noise ratios, $S/N > 2$ ($PI/\sigma_{PI} > 2$) and $S/N > 3$ ($PI/\sigma_{PI} > 3$), where PI is the polarization intensity and σ_{PI} is its uncertainty. In panels (c) and (d) of Figure 2 in A. Soam et al. (2019), the histogram distributions of magnetic field position angles (PA) and polarization fraction (P) show very similar trends for both $S/N > 2$ and $S/N > 3$, which makes to consider the $2 < S/N < 3$ data for further analysis. For our analysis, we use 211 polarization vectors satisfying an $S/N > 2$, the same as used in the study of magnetic field morphology and strength in A. Soam et al. (2019). For the details on data acquisition, reduction, validation, and selection, please refer to Section 2 of A. Soam et al. (2019).

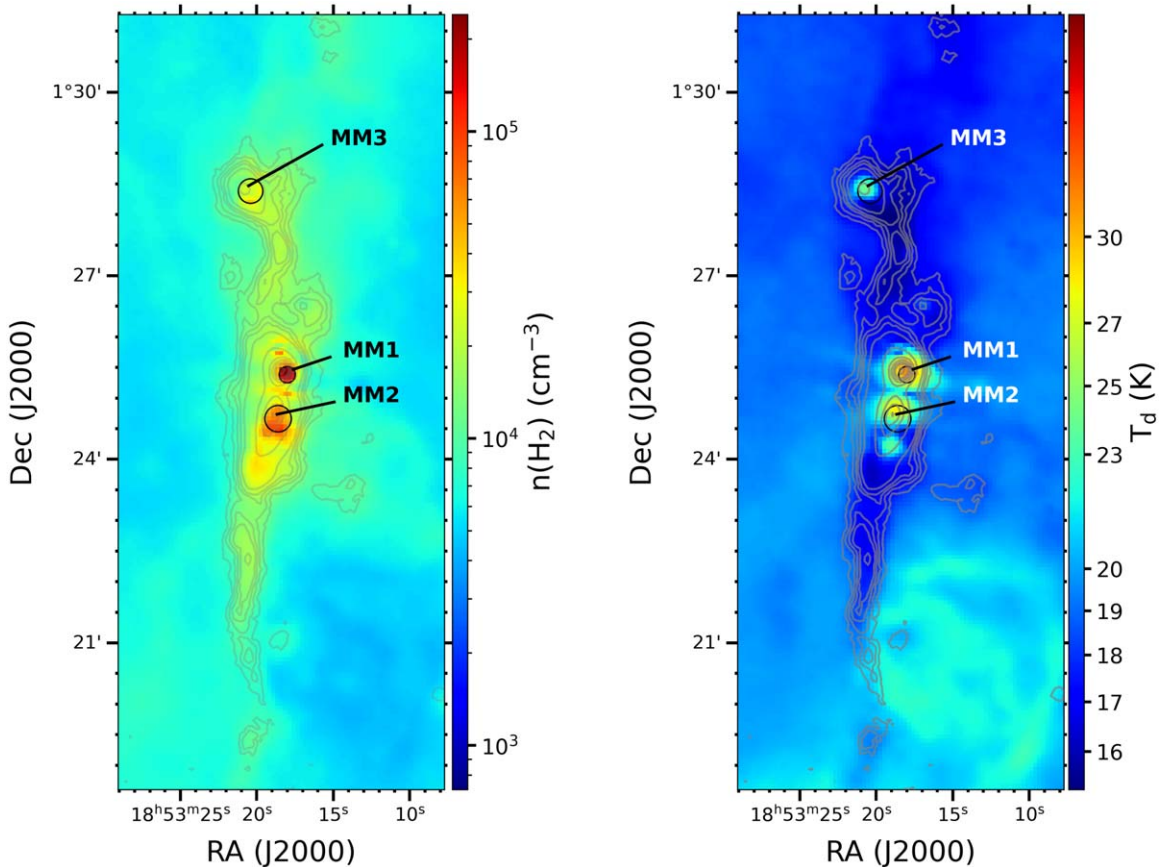


Figure 1. Maps of H_2 volume density (left) and dust temperature (right) for the G34 filament. The locations of the cores MM1, MM2 and MM3 as identified by J. M. Rathborne et al. (2006) are indicated by black circles.

2.2. Maps of H_2 Column Densities, Volume Densities, and Dust Temperatures

We use the H_2 column density and the dust temperature maps of the G34 filament as estimated in A. Soam et al. (2019) using archival Herschel PACS/SPIRE 70, 160, 250, 350, 500 μm and JCMT 850 μm data fitted with a modified blackbody function.

For calculating the H_2 volume densities, we use the column density map. S. Pan et al. (2024) estimated the width of the G34 filament to be ≈ 0.6 pc using the *RadFil* algorithm (C. Zucker & H. H.-H. Chen 2018). For the cores MM1, MM2 in the Center region and MM3 in the North region, the angular FWHM diameters are estimated to be 16'', 26'', and 24'' corresponding to physical FWHM diameters of around 0.19 pc, 0.42 pc, and 0.38 pc, respectively (J. M. Rathborne et al. 2006). We assume a cylindrical geometry of the overall filament so that the depth of the filament is equal to its width. However, we assume the cores to have spherical geometries so that their widths or diameters are equal to their depths. We use 0.6 pc as the depth value for the overall filament except for the core regions and values of 0.19 pc for the MM1 core, 0.42 pc for the MM2 core, and 0.38 pc for the MM3 core to derive the volume densities of the filament. The volume densities $n(H_2)$ are calculated as follows:

$$n(H_2) = \frac{N(H_2)}{d}, \quad (1)$$

where d is the depth of the filament. Also, it is noted that the estimation of the width or depth of filaments is biased based on

the angular resolution of the observations (G. V. Panopoulou et al. 2022). The maps of $n(H_2)$ and T_d are shown in Figure 1. The volume densities are found to be in the range of 10^4 – 10^5 cm^{-3} . The Center region containing the MM1 and MM2 cores has very high gas volume densities of the order of 10^5 cm^{-3} and the region of the MM3 core has volume density of the order of 10^4 cm^{-3} . The dust temperature decreases from the outer regions toward the inner regions of the filament except for the regions of the MM1, MM2, and MM3 cores, which show high temperatures up to around 31 K. Therefore, the dust grains in the regions inside the filament except the MM1, MM2, and MM3 cores are heated only by the diffused interstellar radiation field (ISRF), whereas those in the regions of the MM1, MM2, and MM3 cores are heated by both the ISRF and the internal radiation field from these protostellar cores.

3. Analysis and Results

3.1. Data Analyses

3.1.1. Total Emission Intensity Map

The map of the total emission intensity I of the G34 filament observed by the JCMT/POL-2 instrument at 850 μm is shown in Figure 2. We mark three regions over the filament with three black dotted rectangles as N, C, and S to denote the North, Center, and South regions of the filament, respectively, in the same way as in A. Soam et al. (2019). The positions of the millimeter cores MM1 and MM2 in the Center, and MM3 in the North are also

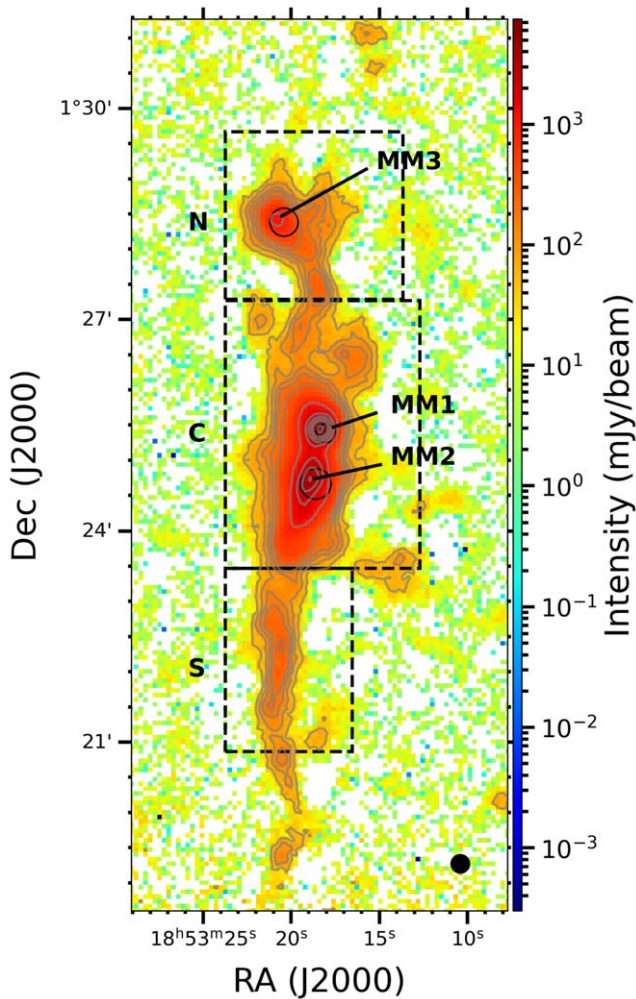


Figure 2. Total emission intensity (I) map of the G34 filament observed by JCMT/POL-2 at $850\ \mu\text{m}$ with overlaid contours drawn at I values of 50, 100, 150, 200, 300, 1000, 2000, 3000, 4000, 5000, 7000 and $8000\ \text{mJy beam}^{-1}$. The positions of three dense millimeter cores MM1, MM2 in the Center region and MM3 in the North region are indicated by black circles. Also, the beam size, $14.1''$ of JCMT/POL-2 at $850\ \mu\text{m}$ is indicated by a solid black circle.

indicated in the figure. The regions of MM1 and MM2 in the Center region show a very high intensity. The MM3 region in the North also shows high intensity but is comparatively lower than the MM1 and MM2 regions. The intensity increases from the outer regions to the inner regions of the filament.

3.1.2. Polarization Fraction Map

The map of the distribution of the polarization vectors observed by JCMT/POL-2 at $850\ \mu\text{m}$ over the G34 filament with $PI/\sigma_{PI} > 3$ in black colors and $2 < PI/\sigma_{PI} < 3$ in green colors is given in Figure 3 (left panel). The lengths of the vectors are proportional to the polarization fraction P and their orientations determine the magnetic field orientations. We find that P becomes smaller and nearly constant in the inner regions where the dust emission intensities are higher and becomes larger in the outer diffused regions of the filament where the intensities are lower. We find high polarization fraction values of 8%–20% in the outer regions having very small Stokes I values. Some outer regions have very high P values going up to around $20\% \pm 6\%$ (typical uncertainty). This feature is also observed in several studies using POL-2 and

HAWC+ observations (e.g., J. Kwon et al. 2018; A. Soam et al. 2018; S. Coudé et al. 2019; K. Pattle et al. 2019; J.-W. Wang et al. 2019; D. Arzoumanian et al. 2021; N. B. Ngoc et al. 2023) and in the protostellar envelopes using ALMA observations (e.g., C. L. H. Hull et al. 2017; W. Kwon et al. 2019). We marked three regions as N, C, and S with three rectangles in the figure indicating the North, Center, and South regions of the filament, respectively, in the same way as we define in Figure 2 to study the grain alignment mechanisms in each of these regions.

The histogram distributions of the polarization fraction P for each region are given in Figure 3 (lower panel). The solid and the dashed green lines are for the North region, magenta lines for the Center region, and black lines for the South region with $S/N > 2$ and $S/N > 3$, respectively. The filled gray color is for all the regions with $S/N > 2$ and the filled orange color is for all the regions with $S/N > 3$. The median polarization fractions for the North, Center, and South regions with $S/N > 2$ are $3.17\% \pm 3.00\%$, $2.93\% \pm 1.89\%$, $6.50\% \pm 2.48\%$ and for $S/N > 3$ are $3.32\% \pm 2.75\%$, $2.68\% \pm 1.21\%$, $6.39\% \pm 1.19\%$, respectively. The median polarization fractions for all the regions with $S/N > 2$ and $S/N > 3$ are $3.41\% \pm 2.58\%$ and $3.29\% \pm 2.29\%$, respectively. The median values for both $S/N > 2$ and $S/N > 3$ are nearly similar.

Figure 4 shows the counts of $P > 15\%$ and $P > 8\%$ in the North, Center, and South regions for different S/N of $PI/\sigma_{PI} > 2, 2.5, 3, 3.5,$ and 4 just to see the trend of high polarization values with increasing S/N . There are some pixels with high P values of around $20\% \pm 6\%$ in the outer regions of the filament but more number in the outer parts of the South region. The Center and North regions have pixels in the outer regions with high P values of more than 8%. The Center region seems to have overall P values lower than those of the North and South regions.

3.1.3. Polarization Fraction as a Function of Total Intensities

In Figure 5, the polarization fraction P is very high, up to nearly 8%–20% in the outer regions having total intensities I less than $60\ \text{mJy beam}^{-1}$ but decreases as I increases toward the filament’s spine. We check the variations of P with I for both $S/N > 2$ and $S/N > 3$. The data for $2 < S/N < 3$ are shown with white facecolors keeping the edgicolors in the same notation as we use to denote the North, Center, and South regions. Also, in the Center region, we identify those data points corresponding to higher dust temperature values of greater than 19.8 K with black edgicolors (see Section 3.1.4 for this particular dust temperature value). The variations of P with I at the regions of North, Center, and South are fitted with weighted power-law fits of the form $P = k_1 I^{a_1}$, where k_1 is a constant and a_1 gives the slope values of the fits as -0.58 ± 0.02 , -0.22 ± 0.00 , and -0.34 ± 0.02 for $S/N > 2$, and -0.58 ± 0.02 , -0.23 ± 0.00 , and -0.30 ± 0.02 for $S/N > 3$ respectively with the uncertainties on the values of a_1 resulting from the best fits. We find that the weighted fits in all the regions for both $S/N > 2$ and $S/N > 3$ are almost similar. Also, since the fit is weighted fit, it mostly favors the higher S/N data with less favor for the lower S/N data. For further analysis in this work, we use $S/N > 2$ data with weighted fits. The overall slope in the Center region is shallower than the North and the South regions. For the Center region, we also fit weighted power-law fits for $I < 850\ \text{mJy beam}^{-1}$ and $I \geq 850\ \text{mJy beam}^{-1}$ with thin and thick gray solid lines giving

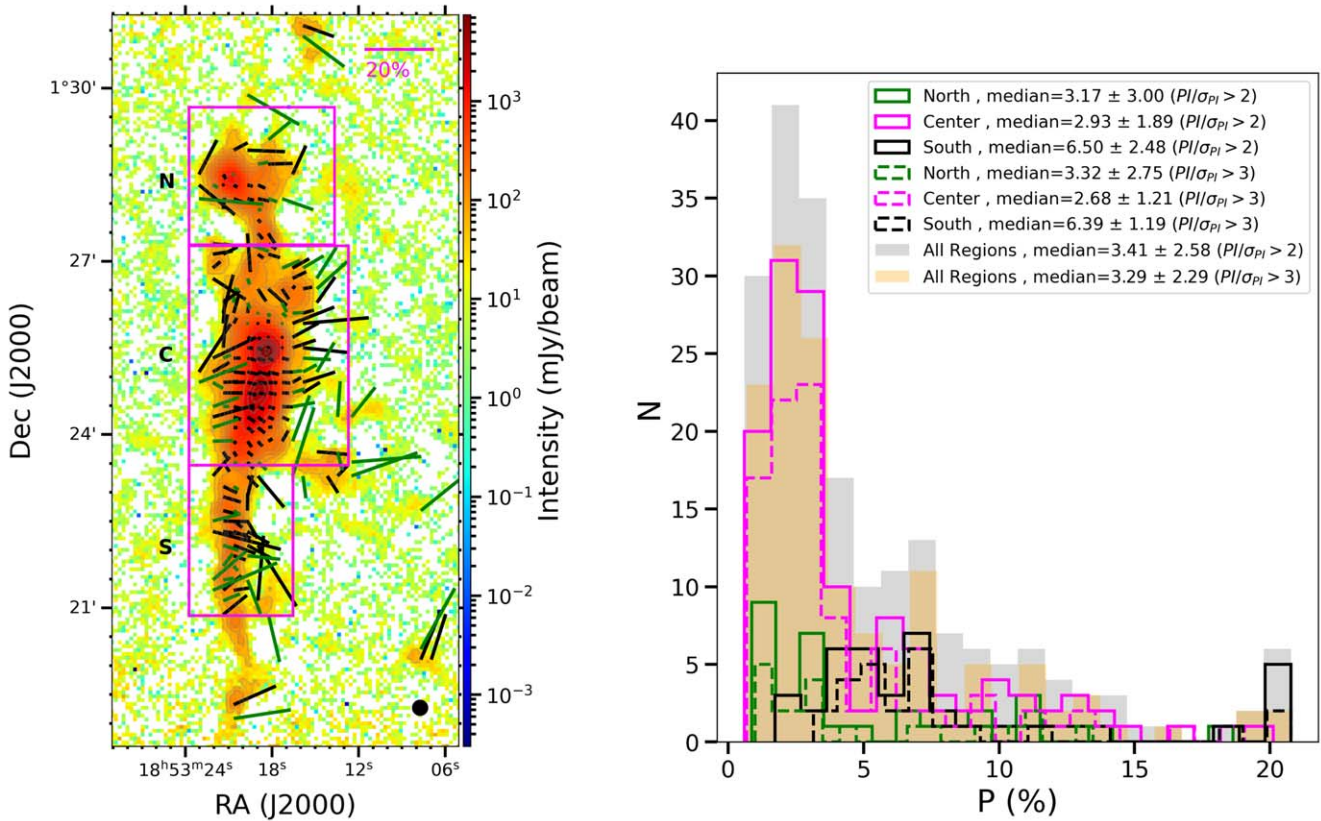


Figure 3. Map of distribution of polarization vectors over all the G34 filament with the black vectors corresponding to $PI/\sigma_{PI} > 3$ and green vectors for $2 < PI/\sigma_{PI} < 3$ (left panel) and histograms of polarization fraction P for the North (green), Center (magenta), South (black) regions with solid lines for $PI/\sigma_{PI} > 2$ and dashed lines for $PI/\sigma_{PI} > 3$, the gray-filled for all regions with $PI/\sigma_{PI} > 2$ and orange-filled for all regions with $PI/\sigma_{PI} > 3$ (right panel). The lengths of the vectors are proportional to P and their orientations determine the magnetic field orientations. A reference scale length of 20% for the polarization fraction is indicated. The contours are the same as in Figure 2.

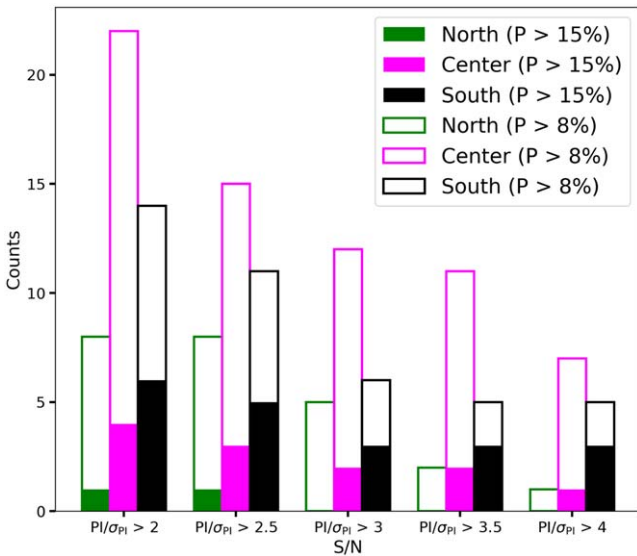


Figure 4. Bar graph showing the counts of $P > 15\%$ and $P > 8\%$ in each region for different S/Ns.

slope values of -0.54 ± 0.01 and -0.36 ± 0.01 , respectively. At this $I = 850 \text{ mJy beam}^{-1}$, there is an increase in P shown with a gray dashed line and then starts decreasing up to a P value of around 0.6%. These may be explained in such a way that the decrease in P up to $850 \text{ mJy beam}^{-1}$ may be associated with the

regions outside the cores and may be due to a decrease in RAT-A efficiency of grains or magnetic field tangling along the line of sight.

The increase in P at around $850 \text{ mJy beam}^{-1}$ may be associated with the grains found in the regions approaching the central cores where the attenuated radiation field from the embedded source favors the alignment of the grains. The decrease in P after $850 \text{ mJy beam}^{-1}$ may be associated with the grains in the regions very near to the central protostar where the internal radiation field strength is very high and may disrupt the large grains in these dense and hot regions (see Figure 12 in T. Hoang et al. 2021). The decrease in P may also be due to the magnetic field tangling along the line of sight.

The parameter a_1 is a very significant parameter that gives information on the grain alignment efficiency variation and magnetic field tangling along the line of sight. Its values in molecular clouds generally range from 0 to 1 (0 for perfect alignment, 1 for no alignment, and between 0 and 1 for some degree of alignment). The most significant source of magnetic field tangling is the turbulence in the cloud (T. J. Jones 1989; T. J. Jones et al. 1992; D. Falceta-Gonçalves et al. 2008).

3.1.4. Polarization Fraction as a Function of Column Densities and Dust Temperatures

Local conditions such as the strength of the radiation field (or equivalently, the dust temperature) and the gas densities play important roles in the variation in the efficiency of grain

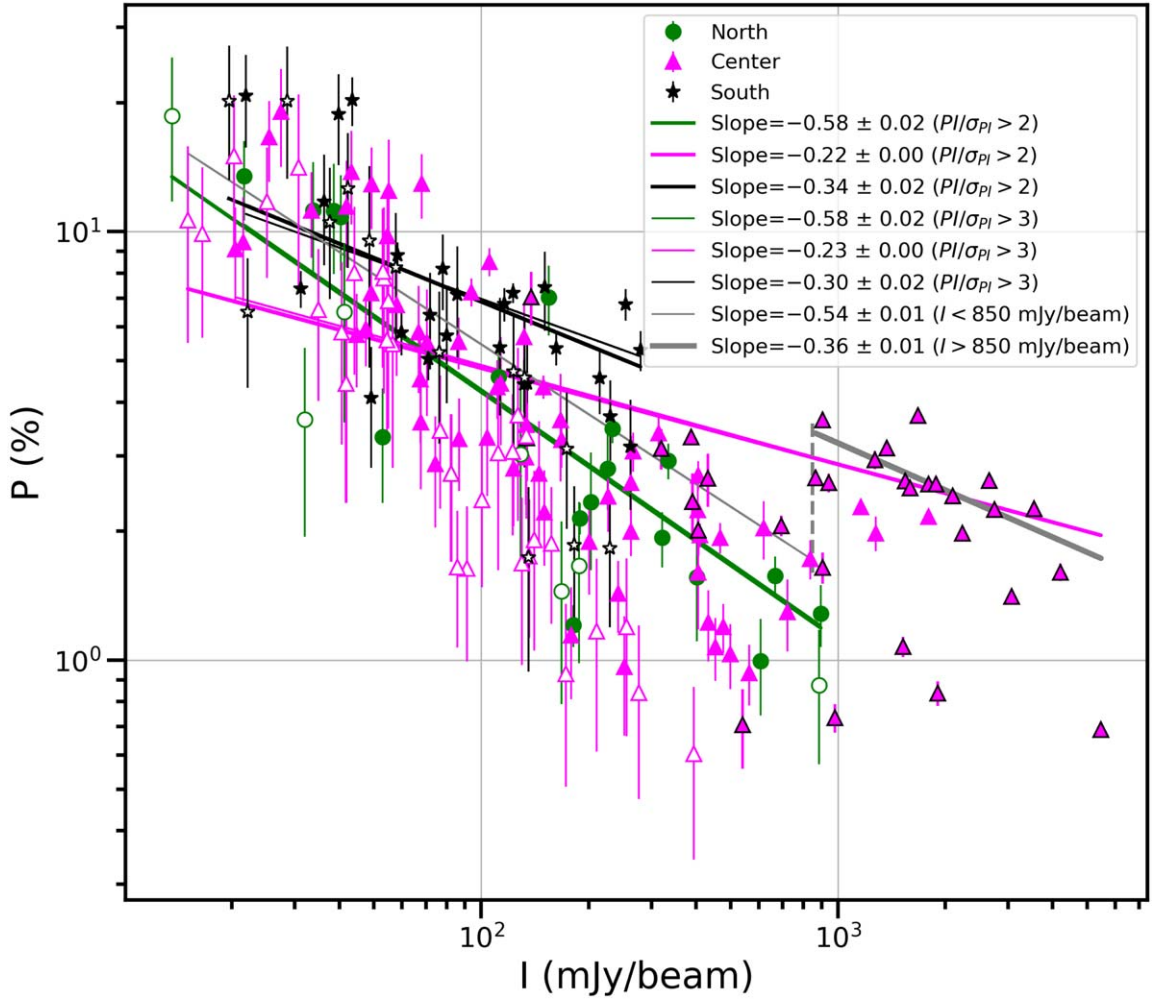


Figure 5. Variations of polarization fractions P with the total intensities I for the North, Center, and South regions. The green, magenta, and black data points are for the North, Center, and South regions with $PI/\sigma_{PI} > 3$ and the white facecolor data points are for $2 < PI/\sigma_{PI} < 3$. The data points in the Center region with $T_d > 19.8$ K are shown with black edgecolors. The solid lines are the weighted best-fit lines for each region with the same color notation. The thin and thick gray solid lines are fitted for $I < 850$ mJy beam $^{-1}$ and $I > 850$ mJy beam $^{-1}$ for the Center region with the gray vertical dashed line to visualize the increase in P at around 850 mJy beam $^{-1}$. P is found to decrease in each of the regions overall.

alignment in accordance with RAT theory (T. Hoang et al. 2021). Therefore, we study the variations of the observed polarization fraction as a function of column density $N(\text{H}_2)$ (Figure 6) and dust temperatures T_d (Figure 7), to find the effects of these local conditions of G34 on the polarization fraction.

We find an anticorrelation in the $P - N(\text{H}_2)$ plot describable by a weighted power-law fit of the form $P = k_2 N(\text{H}_2)^{a_2}$, where k_2 is a constant and a_2 gives a slope with values of -1.18 ± 0.05 for the North region, -0.40 ± 0.01 for the Center region, and -1.13 ± 0.04 for the South region. The overall slope a_2 for the Center region is much shallower than the North and South regions just like we find in the $P-I$ relation in Figure 5. We also fit weighted power-law fits in the Center region for $N(\text{H}_2) < 5 \times 10^{22}$ cm $^{-2}$ and $N(\text{H}_2) \geq 5 \times 10^{22}$ cm $^{-2}$ with thin and thick gray solid lines, giving slope values of -0.83 ± 0.01 and -1.04 ± 0.01 , respectively. We find similar trends with $P-I$ plot in Figure 4. The steep slope in the Center region up to 5×10^{22} cm $^{-2}$ may be associated with the regions outside the cores and after this value may be with the core regions.

In the $P - T_d$ plot, as shown in Figure 7, we find that the polarization fraction P increases with increasing dust temperature in the North up to around 19.8 K and then decreases. For the South region, P only increases with T_d . For the Center region, there is more spread in P up to $T_d = 19.8$ K. However, P increases overall up to around 19.8 K and then decreases with increasing dust temperature, with $T_d = 19.8$ K acting as the transition temperature. However, the polarization fraction decreases more significantly with less spread after around 25 K in the Center region. The variations of P with T_d are fitted with weighted power-law fits of the form $P = k_3 T_d^{a_3}$, where k_3 is a constant and a_3 gives slopes with values of 9.82 ± 0.34 for the North with $T_d < 19.8$ K, 5.42 ± 0.21 for the South, and 0.20 ± 0.12 for the Center with $T_d < 19.8$ K and -1.58 ± 0.02 with $T_d > 19.8$ K. For the Center region, the P values after $I = 850$ mJy beam $^{-1}$ are correlated with those P values after $T_d = 19.8$ K indicated with black edgecolors in Figure 5. Also, P does not drop rapidly initially but as the dust temperature becomes larger around $T_d > 25$ K the value of P significantly decreases. Hence, the subregions in the Center region after 19.8 K are associated with the cores. The increase in polarization fraction with increasing dust temperature is in

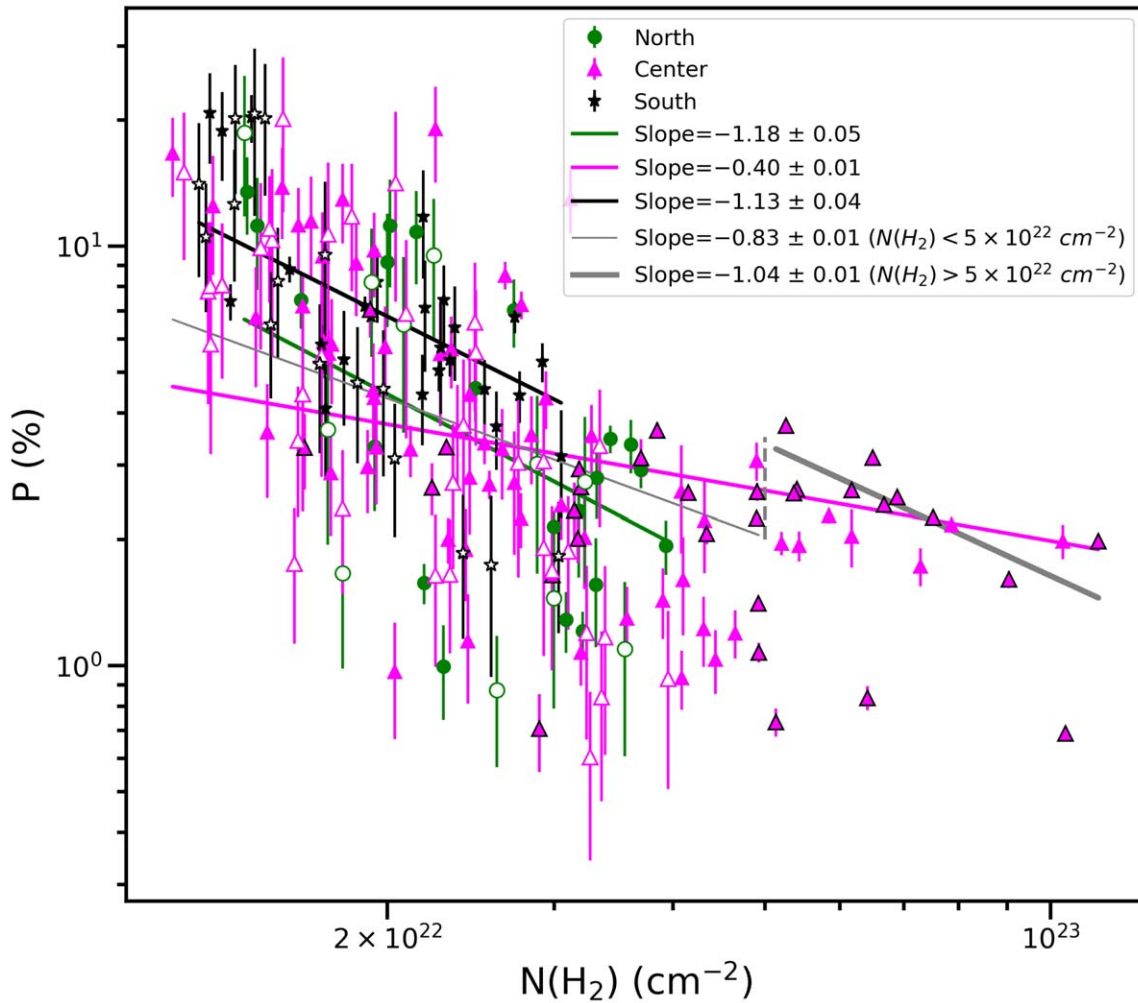


Figure 6. Variations of polarization fractions P with the gas column densities $N(\text{H}_2)$ for the North, Center, and South regions. The thin and thick gray solid lines are the best-fit lines for $N(\text{H}_2) < 5 \times 10^{22} \text{ cm}^{-2}$ and $N(\text{H}_2) > 5 \times 10^{22} \text{ cm}^{-2}$. The gray vertical dashed line is drawn to visualize the increase in P at $N(\text{H}_2) = 5 \times 10^{22} \text{ cm}^{-2}$. The other notations remain the same as in Figure 5. P is found to decrease with $N(\text{H}_2)$ in each of the regions overall like P decreasing with I in Figure 5.

agreement with the prediction of RAT-A theory (H. Lee et al. 2020). However, many observational studies in dense molecular clouds show that the polarization fraction does not always increase with dust temperature. For example, in the study of molecular cloud regions of Aquila Rift, Cham-Musca, Orion, and Ophiuchus in the Gould Belt cloud with the polarization degree measured by the Planck (Planck Collaboration et al. 2020) it was found that P decreases for $T_d > 19$ K. Also, in the study of the molecular cloud Ophiucus A (F. P. Santos et al. 2019; L. N. Tram et al. 2021a), P decreases for $T_d > 25\text{--}32$ K. This feature is found in the North and Center regions of the G34 filament containing dense and hot cores MM3 (North), MM1 and MM2 (Center).

When the radiation strength becomes very strong, large grains can be disrupted into smaller fragments because of the RAT-D effect (T. Hoang et al. 2019). This effect is more efficient in larger grains as RATs are found to be stronger for larger grains (A. Lazarian & T. Hoang 2007; T. Hoang & A. Lazarian 2008). The observed features in the North and Center regions may be explained by RAT-A for the increase in P in the regions outside the cores, whereas a tangled magnetic field along the line of sight due to the large column density

along the line of sight or RAT-D or both may explain the decrease in P for the regions of the embedded cores. We need to disentangle the effect of magnetic field tangling on the depolarization to study the possibility of the RAT-D effect in explaining the depolarization at higher dust temperatures. For the South region with no embedded cores and hence the only radiation field is from the diffused ISRF, the increase in P with increasing T_d may be explained by RAT-A theory.

3.1.5. Effect of Magnetic Field Tangling

The observed polarization fraction depends not only on the dust properties and grain alignment but also on the line-of-sight magnetic field geometry. Turbulence of super-Alfvénic in nature in the cloud can cause magnetic field tangling which can result in the decrease of polarization fraction. But to check whether the observed depolarization as the intensity increases is due to the effect of magnetic field tangling or decrease in net alignment efficiency of grains in denser regions or both, we need to disentangle the effect of magnetic field tangling on depolarization. For this, we calculate the polarization angle dispersion function S and $P \times S$. The value of S provides

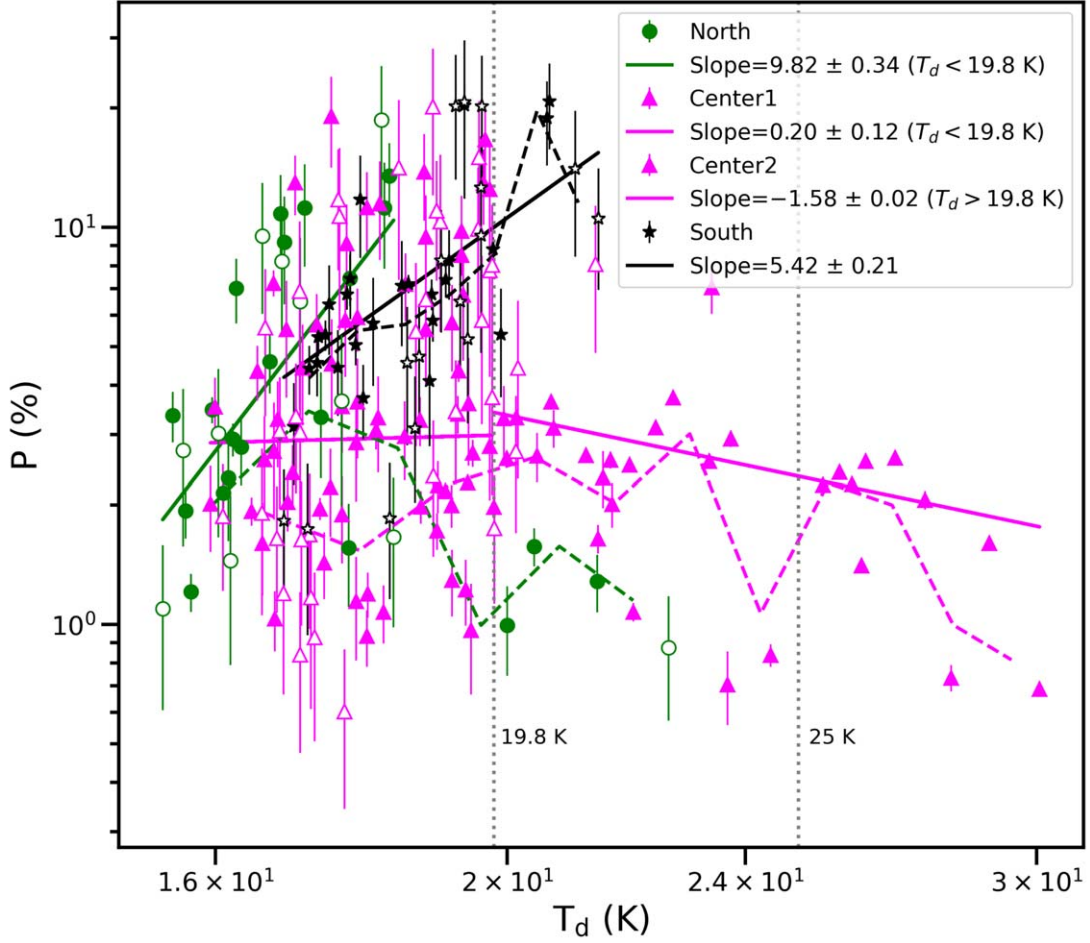


Figure 7. Variations of polarization fractions P with dust temperatures T_d in the North, Center, and South regions. The dashed lines are the running means and the solid lines are the weighted best power-law fits of the respective regions. For the North region, the fit is done only for the data up to 19.8 K. A vertical dotted line is drawn at 19.8 K to mark the observed decrease in P in the North and Center regions. The Center region shows a more significant decrease in P after around 25 K, as shown by another dotted line at 25 K.

information on the local nonuniformity in the distribution of magnetic field morphology. The value of $P \times S$ provides information on the averaged grain alignment efficiency along the line of sight (Planck Collaboration et al. 2020). For a constant grain alignment efficiency, a larger value of S means stronger magnetic field tangling, which would result in a lower value of polarization fraction, and a smaller value means weaker magnetic field tangling, which would give a higher value of polarization fraction.

According to the definition described in Section 3.3 of Planck Collaboration et al. (2020), we calculate S using the following relation:

$$S^2(r, \delta) = \frac{1}{N} \sum_{i=1}^N [\psi(r + \delta_i) - \psi(r)]^2, \quad (2)$$

where the sum extends over the N pixels, indexed by i and located at positions $r + \delta_i$, within a circle centered on r and having radius of δ taken as two times the beam size of JCMT/POL-2. The term $[\psi(r + \delta_i) - \psi(r)]$ is the difference in the polarization angles at positions $r + \delta_i$ and r .

As there are noises on Stokes parameters Q and U , S is biased. This bias of S can be positive or negative based on whether the true value is smaller or larger than the random polarization angle of 52° (D. Alina et al. 2016). An estimate of

the variance of S (σ_S) because of noise and then the debiased S (S_{db}) as described in Section 3.5 of Planck Collaboration et al. (2020) are given by

$$\sigma_S^2(r, \delta) = \frac{\sigma_\psi^2(r)}{N^2 S^2} \left[\sum_{i=1}^N \psi(r + \delta_i) - \psi(r) \right]^2 + \frac{1}{N^2 S^2} \sum_{i=1}^N \sigma_\psi^2(r + \delta_i) [\psi(r + \delta_i) - \psi(r)]^2 \quad (3)$$

and

$$S_{\text{db}}^2(r, \delta) = S^2 - \sigma_S^2 \text{ if } S > \sigma_S. \quad (4)$$

We use only those values of S_{db} with $S > \sigma_S$ and other values not satisfying this condition are removed. Hereafter, we use S to mean $S_{\text{db}}(r, \delta)$ for convenience. Then, we study the variation of P with S , as shown in Figure 8. We fit the weighted running means for each region instead of best-fit lines. The data points show a large spread and best-fit lines do not reflect well the large spread in the data. The weighted running means more clearly show the variations. We find that the North region does not show significant variation of P with S . The Center region shows some slight decreasing nature of P ; however, overall

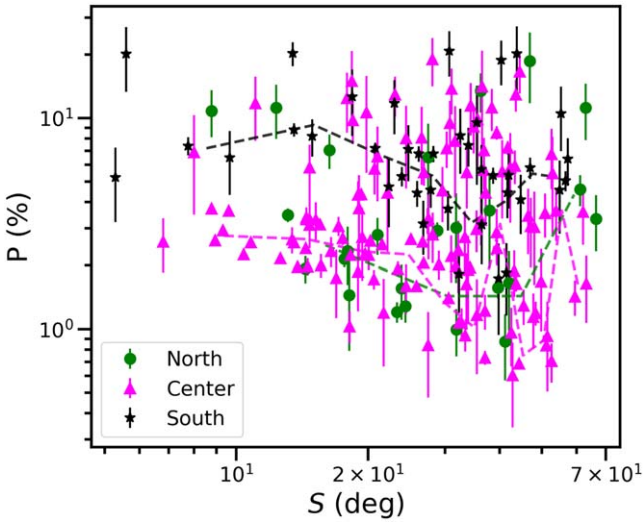


Figure 8. Relation between polarization fraction P and polarization angle dispersion function S in each region.

there is not much significant correlation between P and S . In the South region, we find that P decreases with S .

Again, we study the variation of averaged alignment efficiency $P \times S$ with total intensity I as shown in Figure 9 and find that the alignment efficiency decreases with intensity in the North and Center regions as similar with variations of P with I in Figure 5 but decreases slightly in the South region. The slope for the South region becomes shallower in $P \times S$ variation with I than in P variation with I , which may imply that the magnetic field tangling is significant to cause depolarization in the South region and the slight decrease in averaged alignment efficiency with intensity in the South region can be explained by RAT-A. Also, the decrease in averaged alignment efficiency with intensity in the North and Center regions can be explained predominantly by a decrease in grain alignment efficiency in denser regions.

The variation of $P \times S$ with T_d is shown in Figure 10 and it follows nearly similar to the variation of P with T_d (see Figure 7). The variations of $P \times S$ with $N(\text{H}_2)$ and $N(\text{H}_2)$ with T_d are shown in the left and right panels of Figure 11. In the $N(\text{H}_2) - T_d$ plot, $N(\text{H}_2)$ decreases initially and then increases as T_d increases in the North region, which implies that the high dust temperature region of MM3 has high gas column density. Similarly, the Center region containing MM1 and MM2 has high dust temperatures and gas column densities. In the South region, which does not have embedded protostellar cores, $N(\text{H}_2)$ decreases with T_d . In the variations of $P \times S$ with increasing T_d and $N(\text{H}_2)$, the averaged grain alignment efficiency decreases significantly in the North and Center regions. In the South region, the averaged grain alignment efficiency does not decrease but becomes nearly flat with increasing $N(\text{H}_2)$ but P decreases with increasing $N(\text{H}_2)$ as shown in Figure 6. Hence, the magnetic field tangling effect is significant in the South region and less significant in the North and Center regions.

In the $P \times S$ with T_d plot (Figure 10), the averaged alignment efficiency of grains decreases up to 19.8 K in the Center region when the fitting is a weighted fit. However, up to 19.8 K there is a high spread in the data with a feature of P tending to increase. To study the variations more clearly, we plot weighted running means, which show an initial increase in $P \times S$ and then decrease at higher T_d values. After 19.8 K, the spread becomes

less and the grain alignment efficiency decreases. In the North region, the grain alignment efficiency increases up to 19.8 K and then decreases. In the South region, the grain alignment efficiency slightly increases in the weighted fit but increases overall in the weighted running means at higher T_d values. This variation of $P \times S$ with T_d is nearly similar to the variation of P with T_d as shown in Figure 7 for the North and Center regions but the South region shows a shallower slope. The magnetic field tangling seems to have some role in causing depolarization in the South region. In the North and Center regions, the decrease in averaged alignment efficiency of grains at larger dust temperature values may imply the possibility of the effect of RAT-D in the protostellar core regions of MM3 (North) and MM1 and MM2 (Center), which have high T_d values due to the presence of high internal radiation fields from the central protostars embedded in these cores.

3.2. Grain Alignment and Disruption Mechanisms

3.2.1. Minimum Alignment Size of Grains

The study of grain sizes is very important as far as RAT theory is concerned in the study of grain alignment mechanisms. From RAT-A theory, effective alignment of grains can be achieved only when they can rotate with a rate far more than the thermal rotation rate, i.e., suprathermal rotation (T. Hoang & A. Lazarian 2008, 2016) so that the randomization of grains by gas-grain collisions can be neglected. The dust polarization fraction is determined by the size distribution of aligned grains, spanning from a minimum size of aligned grains, hereafter alignment size, a_{align} to the maximum grain size, a_{max} (T. Hoang & A. Lazarian 2014; H. Lee et al. 2020). We use the following relation as given in T. Hoang et al. (2021) to calculate the values of a_{align} in all the regions of the filament:

$$a_{\text{align}} \simeq 0.055 \hat{\rho}^{-1/7} \left(\frac{\gamma U}{0.1} \right)^{-2/7} \left(\frac{n_{\text{H}}}{10^3 \text{ cm}^{-3}} \right)^{2/7} \times \left(\frac{T_{\text{gas}}}{10 \text{ K}} \right)^{2/7} \left(\frac{\bar{\lambda}}{1.2 \mu\text{m}} \right)^{4/7} (1 + F_{\text{IR}})^{2/7}, \quad (5)$$

where $\hat{\rho} = \rho_d / (3 \text{ g cm}^{-3})$ with ρ_d being the dust mass density; γ is the anisotropy degree of the radiation field; $\bar{\lambda}$ represents the mean wavelength of the radiation; U is the radiation field strength; n_{H} is the number density of hydrogen atoms; T_{gas} is the gas temperature; and F_{IR} is the ratio of the IR damping to the collisional damping rate. We take $\gamma = 0.3$ for the regions outside the MM1, MM2, and MM3 cores as the radiation becomes more anisotropic in elongated dense filamentary clouds (B. T. Draine & J. C. Weingartner 1997; T. J. Bethell et al. 2007). However, for the protostellar cores MM1, MM2, and MM3, we take $\gamma = 1$ as the radiation field is dominated by the internal radiations from the high-mass and high-luminosity central protostars and the radiation field becomes unidirectional within these core regions. We use $\rho_d = 3 \text{ g cm}^{-3}$, $\bar{\lambda} = 1.2 \mu\text{m}$, and $n_{\text{H}} = 2n(\text{H}_2)$ where $n(\text{H}_2)$ is the volume density of molecular hydrogen gas and $T_{\text{gas}} = T_d$ is considered as this thermal equilibrium between gas and dust is valid for dense and cold environments. For dense molecular clouds, $F_{\text{IR}} \ll 1$. To calculate U , we use the relation between dust temperature and the radiation strength for silicate grains having sizes in the range of 0.01–1 μm with dust heating and cooling balance and radiation strength $U < 10^4$ ($\approx 75 \text{ K}$), i.e., $U \approx (T_d / 16.4 \text{ K})^6$

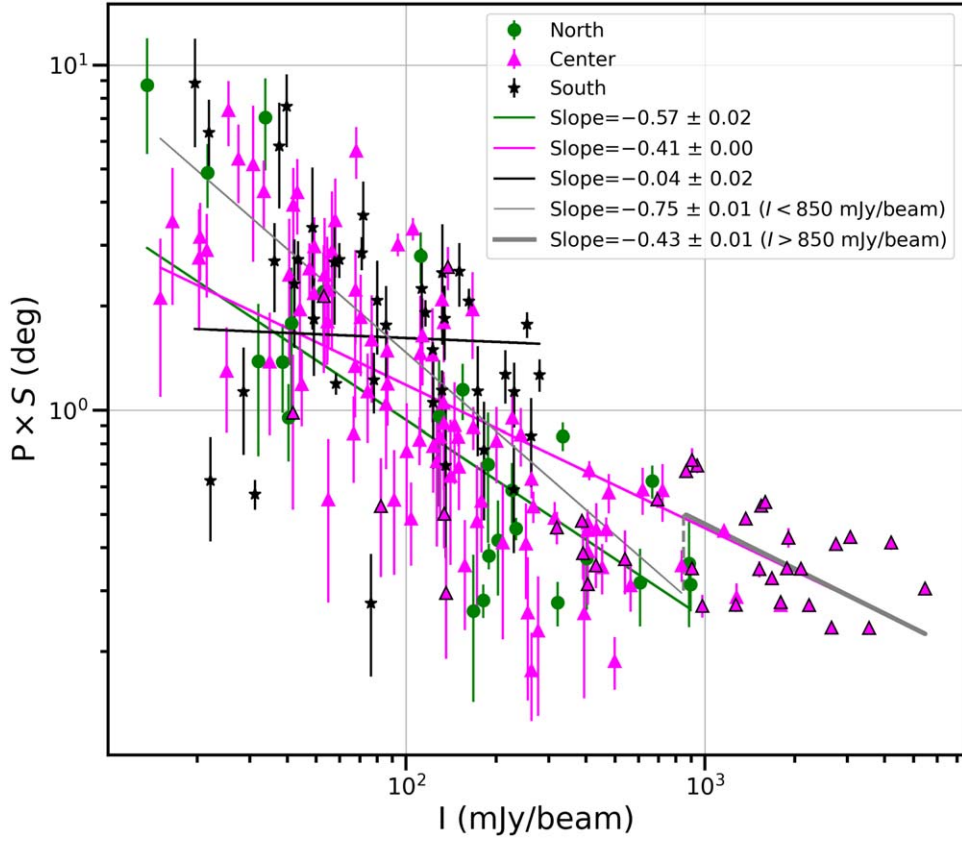


Figure 9. Variation of averaged grain alignment efficiency $P \times S$ with the total intensity I in each region. All the notations are the same as in Figure 5.

(B. T. Draine 2011). The map of the alignment size is given in the left panel of Figure 12. We find that the alignment size increases from the outer layer to the inside in the filament for the North region, except for the region of MM3, which shows a significant reduction in alignment size, and the South region, except for the region containing MM1 and MM2 in the Center region, the alignment size significantly decreases.

In the context of the RAT paradigm, aligned grains have their size distributions ranging from a_{align} to a_{max} and the polarization fraction is determined by this range of grain size distributions. The value of a_{max} is determined by grain growth and destruction processes. When a certain a_{max} is given, increasing the value of a_{align} can result in a narrower size distribution of aligned grains, which can reduce polarization fraction P . Also, decreasing the value of a_{align} can result in a wider size distribution of aligned grains, which can give a higher P (see Figure 7 in L. N. Tram & T. Hoang 2022). So, it is expected to get an anticorrelation between a_{align} and P . Also, it is expected that a_{align} should increase with I in starless clouds.

Figure 13 shows the variation of a_{align} with total emission intensity I . The North and South regions show nearly similarly an increase in a_{align} as I increases up to $350 \text{ mJy beam}^{-1}$, which means that a_{align} increases in denser regions and then the North region shows a decrease in a_{align} , which could be due to the presence of dense and hot core MM3.

The Center region shows an increase in a_{align} at first up to around $850 \text{ mJy beam}^{-1}$ but at higher intensity values a_{align} decreases, which can be due to the presence of internal radiations from the cores MM1 and MM2. The modeling of grain alignment and grain disruptions in very dense protostellar

cores, as given in T. Hoang et al. (2021), shows that because of the effect of the stellar radiation field a_{align} first changes slowly in the envelope and then decreases rapidly when entering the region around the protostar due to the increase in radiation flux and constant gas density. In the presence of these protostars, the grains can be disrupted by RATs into smaller fragments and it can decrease P . Figure 14 shows the variation of P (left) and $P \times S$ (right) with a_{align} . We plot weighted power-law fit and also weighted running means for the regions up to $350 \text{ mJy beam}^{-1}$ for the North region and up to $850 \text{ mJy beam}^{-1}$ for the Center region. The data points after these values are indicated with black edgicolors.

It is found that the value of polarization fraction P and averaged grain alignment efficiency $P \times S$ decreases in the North region significantly and shows some spread in the Center and South regions but decreases overall at higher a_{align} values. Polarization fraction decreases as a_{align} increases due to the reduction in the fraction of aligned grains, from numerical modeling (H. Lee et al. 2020; T. Hoang et al. 2021). These features in the North and Center regions may be associated with the regions outside the cores. The other data points shown in black edgicolors that correspond to $I > 350 \text{ mJy beam}^{-1}$ for the North region and $I > 850 \text{ mJy beam}^{-1}$ for the Center region show small P and $P \times S$ values overall. At smaller a_{align} values, we expect a higher polarization fraction but the P and $P \times S$ values are small even at smaller a_{align} values for these intensity values. These data points may be associated with the regions of the cores. The decrease in the polarization fraction at smaller a_{align} values is opposite to the expectation of RAT-A theory. Therefore, we expect the possibility of the RAT-D effect in these protostellar cores.

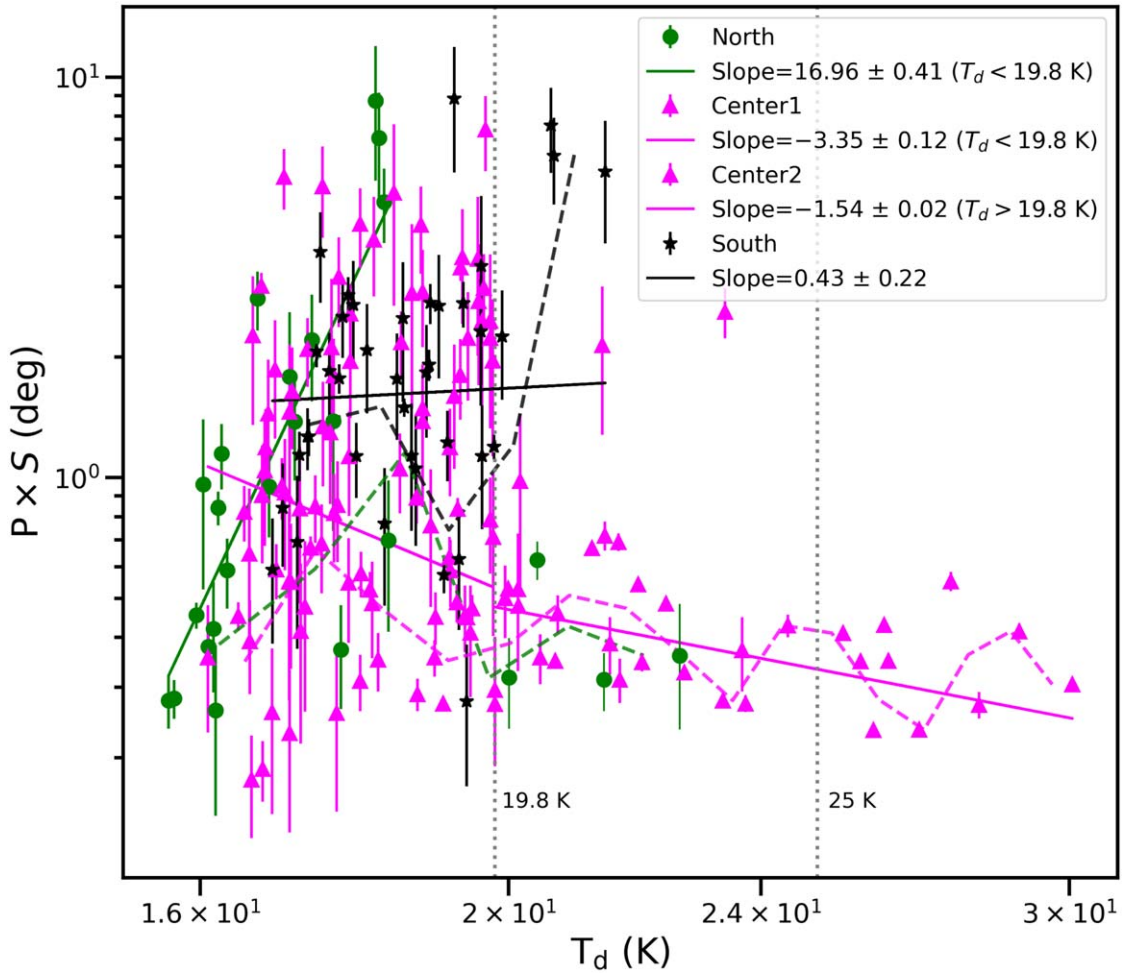


Figure 10. Variations of the averaged grain alignment efficiency $P \times S$ with dust temperature T_d in each region. All the notations are the same as in Figure 7.

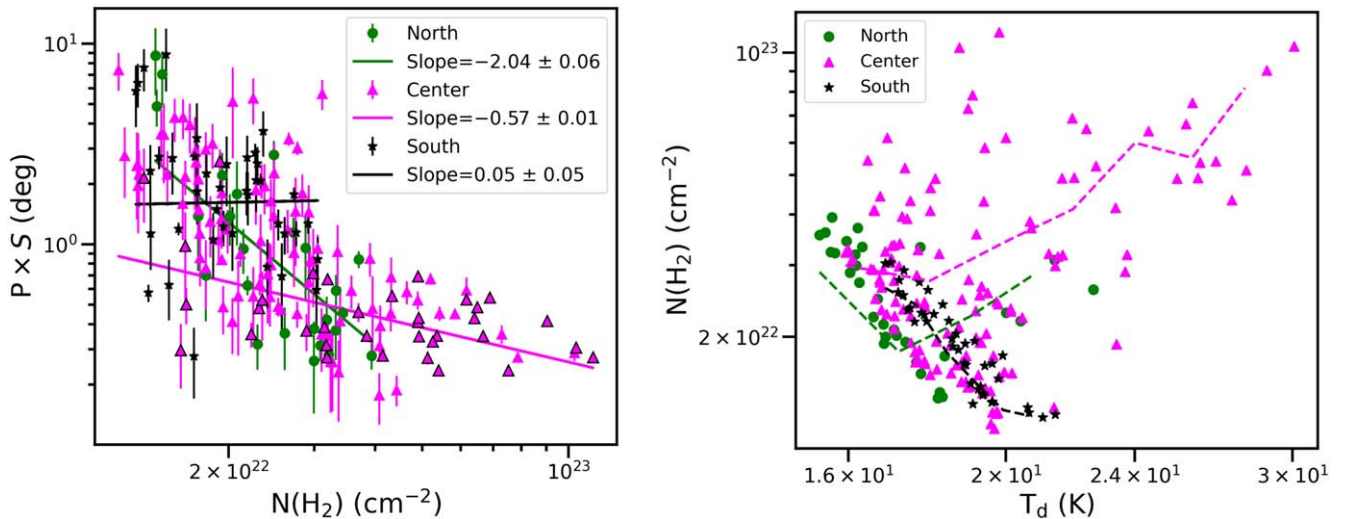


Figure 11. Variations of the averaged grain alignment efficiency $P \times S$ with the gas column density $N(\text{H}_2)$ (left) and $N(\text{H}_2)$ with dust temperature T_d (right) in each region.

3.2.2. Minimum Disruption Size of Grains

The depolarization with increasing T_d may also be caused by the fluctuations in the average B -field orientations along the line of sight within the unresolved cores. There have been

many studies to investigate the B -fields in G34 filament at different wavelengths with dust and line emission polarization observations. For example, the mapping of the B -field morphologies in the region of the MM1 and MM2 cores has

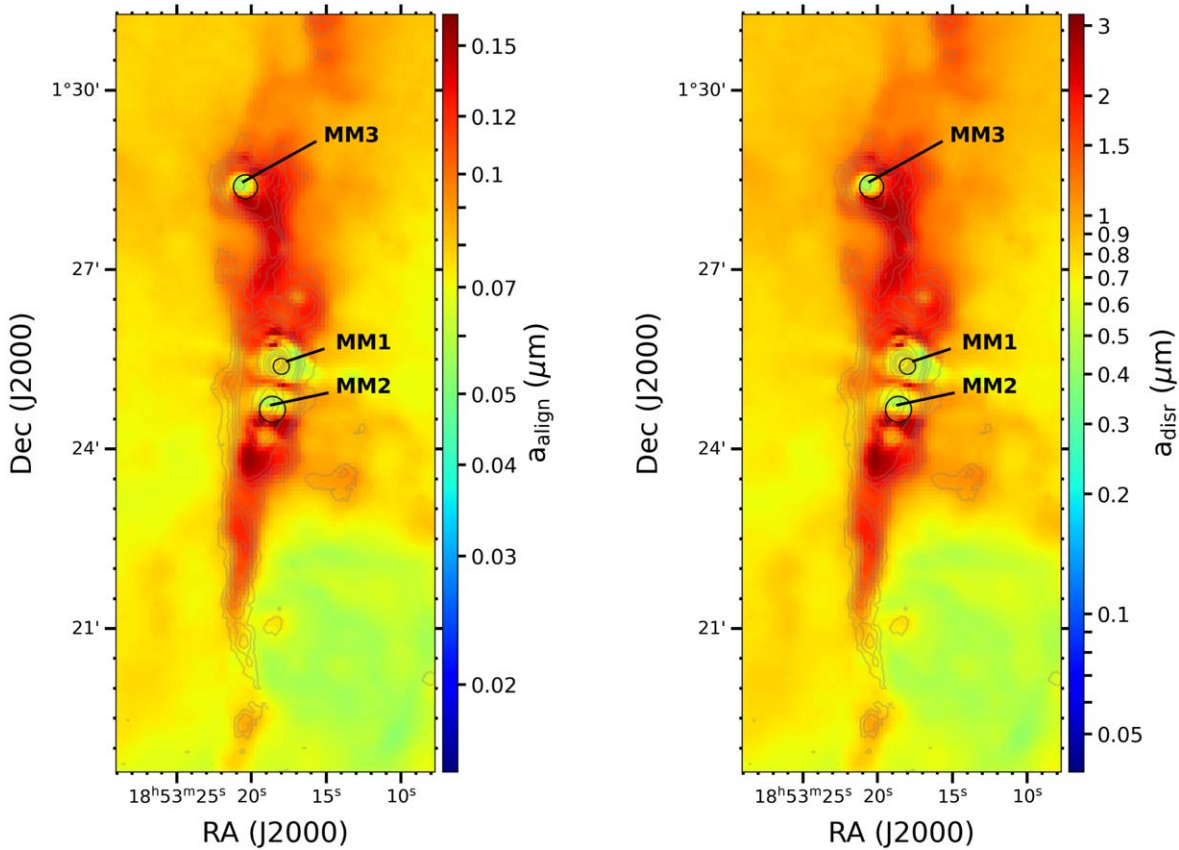


Figure 12. Maps of minimum alignment size, a_{align} (left) and minimum disruption size, a_{disr} (right).

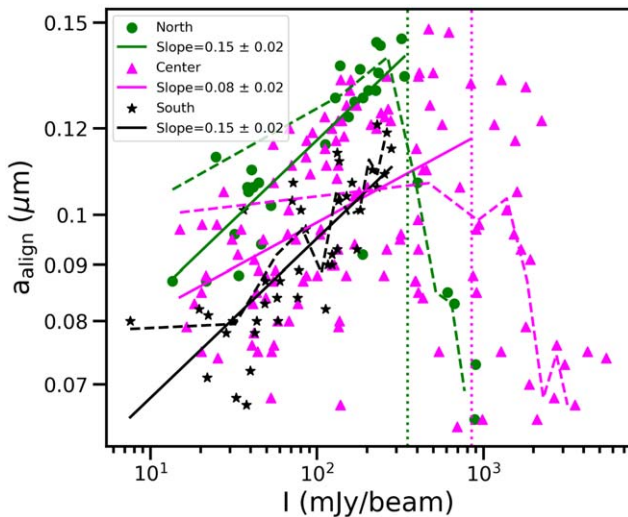


Figure 13. Variation of a_{align} with I . The dashed lines are the running means and the solid lines are the best-fit lines of the respective regions. The best-fit lines for the North and Center regions are fitted only up to $I = 350$ mJy beam^{-1} and $I = 850$ mJy beam^{-1} marked with vertical green and magenta dotted lines, respectively.

been done using dust polarization observations by JCMT/POL-2 at $850 \mu\text{m}$ with $14''.1$ resolution (A. Soam et al. 2019), TADPOL/Combined Array for Research in Millimeter-wave Astronomy at 1.3 mm with $2''.5$ resolution (C. L. H. Hull et al. 2014), and Submillimeter Array (SMA) at $870 \mu\text{m}$ with $1''.5$ resolution (Q. Zhang et al. 2014). A comparison of the B -field morphologies mapped by these different observations in the

MM1 and MM2 core regions is given in Figure 9 of A. Soam et al. (2019). The SMA observations show deviation in the B -field orientations from the JCMT/POL-2 observations in these cores. However, in all these observations, the B -field orientations in these core regions are almost uniform. Therefore, the contribution from the magnetic field tangling along the line of sight on the observed depolarization in these dense cores is expected to be small. The depolarization with increasing T_d in the North and Center regions may also be caused by B -field tangling and/or a change in the B -field inclination angle within the unresolved beam (T. Hoang & B. Truong 2024). However, there is a lack of details on the B -field tangling and inclination variation. Here, we explore whether RAT-D can happen in these warm environments associated with the cores MM1 and MM2 in the Center region and MM3 in the North region and explain the observed depolarization by estimating the minimum disruption size of grains. Since the MM1 and MM2 cores have high bolometric luminosities of the order of $10^4 L_\odot$ with masses of $433 M_\odot$ and $533 M_\odot$, respectively, and MM3 of the order of nearly $10^3 L_\odot$ with mass of $171 M_\odot$ which may imply the presence of high-mass protostars (J. M. Rathborne et al. 2010), the possibility of occurring RAT-D in these hot and dense cores is expected to be high.

As mentioned in the introduction in Section 1, when exposed to a very high radiation field, large grains could be disrupted into smaller fragments when the centrifugal stress induced by rapid rotation exceeds the tensile strength of the grains, termed the RAT-D mechanism. The grain disruption depends on their tensile strength, denoted by S_{max} , which is an uncertain parameter determined by their structure and composition. Composite grains have $S_{\text{max}} \approx 10^6 - 10^7 \text{ erg cm}^{-3}$ and compact

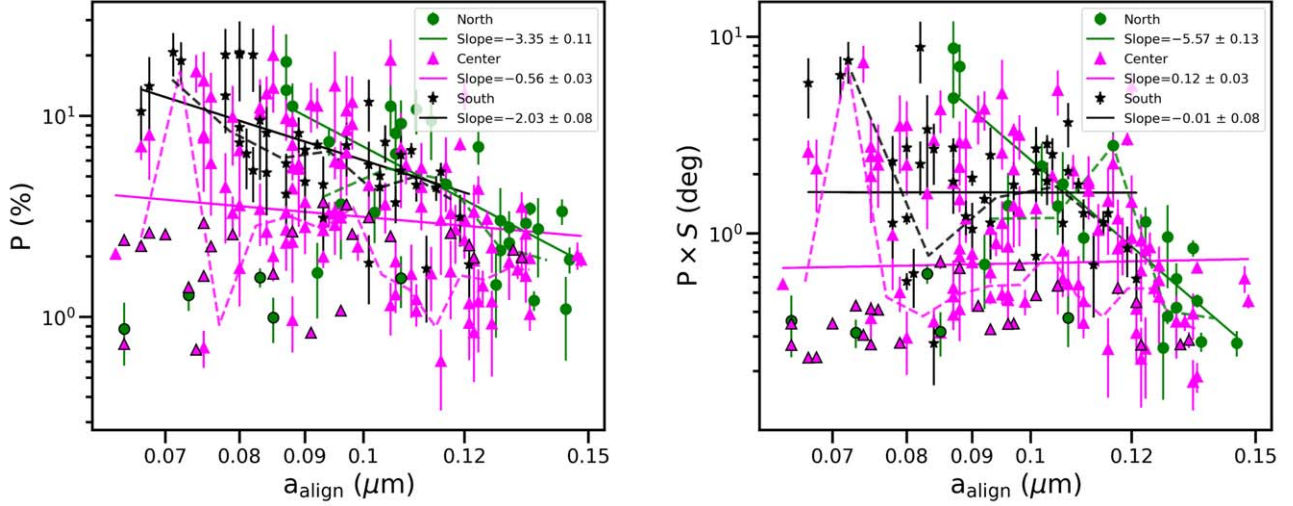


Figure 14. Variations of P with a_{align} (left) and $P \times S$ with a_{align} (right) in each of the regions. The dashed lines are the weighted running means and the solid lines are the weighted best-fit lines. For the North and Center regions, the running means and the fits are done only for $I < 350 \text{ mJy beam}^{-1}$ and $I < 850 \text{ mJy beam}^{-1}$, respectively. The data points after these I values are shown with black edgecolors.

grains have $S_{\text{max}} \approx 10^9 - 10^{11} \text{ erg cm}^{-3}$ (T. Hoang et al. 2019). In dense molecular clouds, grains are expected to be large and have composite structures due to grain coagulation processes. The disruption of grains by the RAT-D mechanism decreases the observed polarization fraction due to the depletion of large grains. We calculate the minimum size of grains that can be disrupted, known as disruption size, a_{disr} , using the analytical formula given in T. Hoang et al. (2021) as follows:

$$a_{\text{disr}} \approx 1.7 \left(\frac{\gamma_{-1} U}{n_3 T_1^{1/2}} \right)^{-1/2} \left(\frac{\bar{\lambda}}{1.2 \mu\text{m}} \right) \hat{\rho}^{-1/4} S_{\text{max}}^{1/4} \times (1 + F_{\text{IR}})^{1/2} \mu\text{m}. \quad (6)$$

The a_{disr} value depends on the local gas properties, the strength of the radiation field and the grain tensile strength. For our calculation of a_{disr} , we consider $S_{\text{max}} = 10^5 \text{ erg cm}^{-3}$ for

large porous composite grains that are expected in dense regions of the filament due to grain coagulation processes. From the numerical simulations for porous grain aggregates by M. Tatsuuma et al. (2019), the parameter S_{max} can be calculated using the analytical formula given in Equation (33) in M. Tatsuuma et al. (2019). For large composite grains made up of monomers (constituent particles) of radius $0.1 \mu\text{m}$, volume filling factor of 0.1, and surface energy per unit area of the material of 10^2 erg cm^{-2} , $S_{\text{max}} \approx 10^5 \text{ erg cm}^{-3}$. The other parameter values are taken the same as those used in the calculation of a_{align} in Equation (5). The map of the minimum disruption size thus calculated is shown in the right panel of Figure 12. The histogram distributions of the minimum alignment and disruption sizes of grains for each region are shown in the left and the right panels of Figure 15. In the left panel, the green and magenta vertical dotted lines denote the

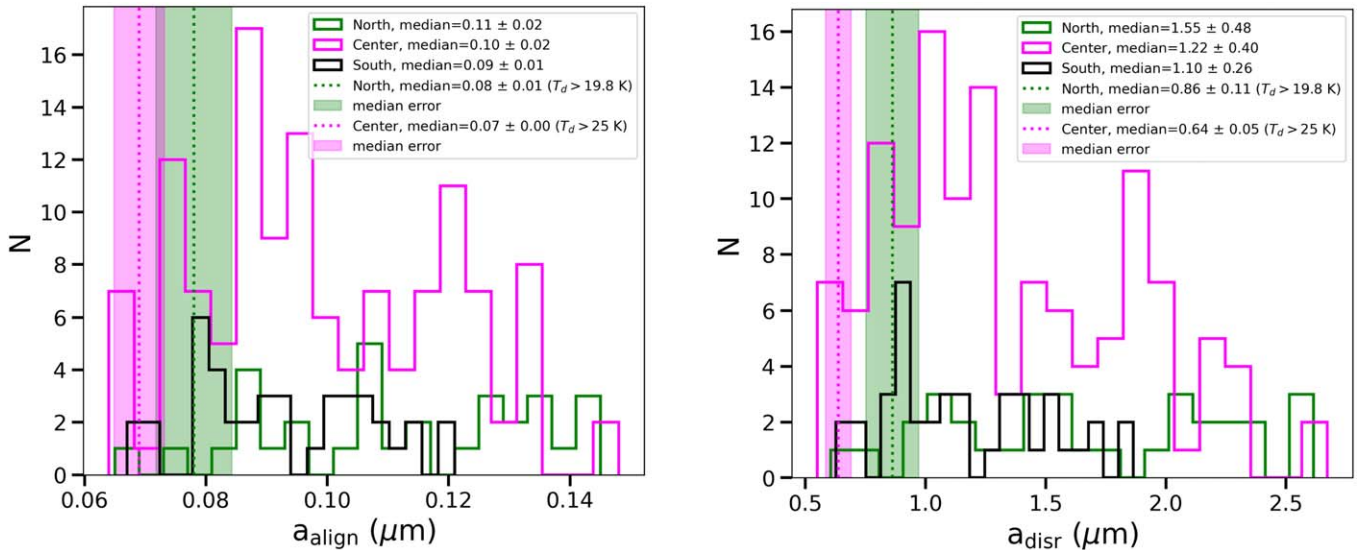


Figure 15. Histogram distributions of a_{align} (left panel) and a_{disr} (right panel) for each of the North, Center, and South regions. The vertical green and magenta dotted lines in each panel represent the median values for the North region with $T_d > 19.8 \text{ K}$ and the Center region with $T_d > 25 \text{ K}$ and the shaded regions the corresponding uncertainties in the median values, respectively.

Table 1
Slope Values of Weighted Power-law Fits for Different Analyses Using $PI/\sigma_{PI} > 2$

Relation	North	Center	South
P versus I	-0.58 ± 0.02	-0.22 ± 0.00 (overall I) -0.54 ± 0.01 ($I < 850$ mJy beam $^{-1}$) -0.36 ± 0.01 ($I > 850$ mJy beam $^{-1}$)	-0.34 ± 0.02
P versus $N(\text{H}_2)$	-1.18 ± 0.05	-0.40 ± 0.01 (overall $N(\text{H}_2)$) -0.83 ± 0.01 ($N(\text{H}_2) < 5 \times 10^{22}$ cm $^{-2}$) -1.04 ± 0.01 ($N(\text{H}_2) > 5 \times 10^{22}$ cm $^{-2}$)	-1.13 ± 0.04
$P \times S$ versus I	-0.57 ± 0.02	-0.41 ± 0.00 (overall I) -0.75 ± 0.01 ($I < 850$ mJy beam $^{-1}$) -0.43 ± 0.01 ($I > 850$ mJy beam $^{-1}$)	-0.04 ± 0.02
P versus T_d	9.82 ± 0.34 ($T_d < 19.8$ K)	0.20 ± 0.12 ($T_d < 19.8$ K) -1.58 ± 0.02 ($T_d > 19.8$ K)	5.42 ± 0.21
$P \times S$ versus T_d	16.96 ± 0.41 ($T_d < 19.8$ K)	-3.35 ± 0.12 ($T_d < 19.8$ K) -1.54 ± 0.02 ($T_d > 19.8$ K)	0.43 ± 0.22
a_{align} versus I	0.15 ± 0.02 ($I < 350$ mJy beam $^{-1}$)	0.08 ± 0.02 ($I < 850$ mJy beam $^{-1}$)	0.15 ± 0.02
P versus a_{align}	-3.35 ± 0.01 ($I < 350$ mJy beam $^{-1}$)	-0.56 ± 0.03 ($I < 850$ mJy beam $^{-1}$)	-2.03 ± 0.08
$P \times S$ versus a_{align}	-5.57 ± 0.13 ($I < 350$ mJy beam $^{-1}$)	0.12 ± 0.03 ($I < 850$ mJy beam $^{-1}$)	-0.01 ± 0.08

median a_{align} value of $0.08 \pm 0.01 \mu\text{m}$ for the North region with $T_d > 19.8$ K and of $0.07 \mu\text{m}$ for the Center region with $T_d > 25$ K and the shaded regions denote the uncertainties in these median values, respectively. Similarly, in the right panel, the green and magenta vertical dotted lines denote the median a_{disr} value of $0.86 \pm 0.11 \mu\text{m}$ for the North region with $T_d > 19.8$ K and of $0.64 \pm 0.05 \mu\text{m}$ for the Center region with $T_d > 25$ K and the shaded regions show the uncertainties in these median values, respectively. The regions of MM3 (North) and MM1 and MM2 (Center) show a significant decrease in values which reach up to nearly $0.6 \mu\text{m}$ at high dust temperatures and the other regions of the filament show the a_{disr} values above $1 \mu\text{m}$.

Figure 16 shows the variations of a_{align} (green) and a_{disr} (magenta) as a function of dust temperatures for the North (left panel) and Center (right panel) regions, with the gray points denoting the respective values after 19.8 K for the North region and after 25 K for the Center region, which act as the transition temperatures (for the Center region, though the P decreases after 19.8 K the more significant decrease in P occurs after around 25 K) (see Figure 7), we find that the disruption and the alignment sizes are large for $T_d < 19.8$ K in the North region and $T_d < 25$ K in the Center region but decrease and become nearly constant after 19.8 K and 25 K, respectively. When $T_d > 19.8$ K, the median value of $a_{\text{align}} \approx 0.08 \pm 0.01 \mu\text{m}$ and median value of $a_{\text{disr}} \approx 0.86 \pm 0.11 \mu\text{m}$ in the North region. When $T_d > 25$ K in the Center region, the median value of $a_{\text{align}} \approx 0.07 \mu\text{m}$ and of $a_{\text{disr}} \approx 0.64 \pm 0.05 \mu\text{m}$. Therefore, larger grains above $0.86 \mu\text{m}$ in the North for the regions of $T_d > 19.8$ K and above $0.64 \mu\text{m}$ for the regions of $T_d > 25$ K in the Center region can be disrupted, thereby resulting in narrower size distributions of grains that can be aligned and hence reduction in the polarization fraction. Also, P and $P \times S$ decrease with T_d for $T_d > 19.8$ K and $T_d > 25$ K in the North and Center regions, respectively (see Figures 7, 10). This can imply the possibility of RAT-D in the dense and hot core regions of the North and Center regions (see Section 4.2 for a discussion).

For all the above analyses, the slope values of the weighted best power-law fits for each of the regions are given in Table 1. The median values of a_{align} and a_{disr} for each of the regions are given in Table 2.

Table 2
Median Values of Minimum Grain Alignment and Disruption Sizes, Mean Values of Magnetic Field, and Median Values with Ranges of Magnetic Relaxation Strengths in the North, Center, and South Regions

Parameters	North	Center	South
a_{align}	$0.08 \pm 0.01 \mu\text{m}$ ($T_d > 19.8$ K)	$0.07 \mu\text{m}$ ($T_d > 25$ K)	$0.09 \pm 0.01 \mu\text{m}$
a_{disr}	$0.86 \pm 0.11 \mu\text{m}$ ($T_d > 19.8$ K)	$0.64 \pm 0.05 \mu\text{m}$ ($T_d > 25$ K)	$1.10 \pm 0.26 \mu\text{m}$
B_{POS}^a	$100 \pm 40 \mu\text{G}$	$470 \pm 190 \mu\text{G}$	$60 \pm 34 \mu\text{G}$
B_{TOT}^a	$130 \pm 52 \mu\text{G}$	$611 \pm 247 \mu\text{G}$	$78 \pm 44 \mu\text{G}$
Median $\delta_{\text{mag,sp}}$	14.66	293.09	6.32
Range of $\delta_{\text{mag,sp}}$	9–25	35–590	5–9

Note.

^a B_{POS} values are taken from A. Soam et al. (2019) and B_{TOT} values are calculated using the relation from R. M. Crutcher et al. (2004).

3.3. Effect of Magnetic Relaxation on RAT-A

In the study of grain alignment, the magnetic properties of dust are very important as they enable the grains to interact with the external magnetic field. When iron atoms are distributed diffusely within a silicate grain, the grain acts as an ordinary paramagnetic material, but when distributed as clusters, the grain becomes super-paramagnetic (T. Hoang et al. 2022a). A paramagnetic grain rotating with an angular velocity ω in an external magnetic field B experiences paramagnetic relaxation (L. J. Davis & J. L. Greenstein 1951) that induces the dissipation of the grain rotational energy into heat, resulting in the gradual alignment of angular velocity and angular momentum with B . This classical Davis–Greenstein mechanism can be applied to any magnetic material. However, the paramagnetic relaxation alone cannot produce an efficient alignment of grains due to gas randomization. Also, only RATs cannot produce perfect alignment of grains because of the dependence of RAT-A efficiency on various parameters like the angle between the direction of radiation and the magnetic field, the shape of the grains and their compositions (T. Hoang & A. Lazarian 2016; J. Herranen et al. 2021). Therefore, to explain the observed high polarization fraction of 8%–20% in the filament, it is important to consider super-paramagnetic

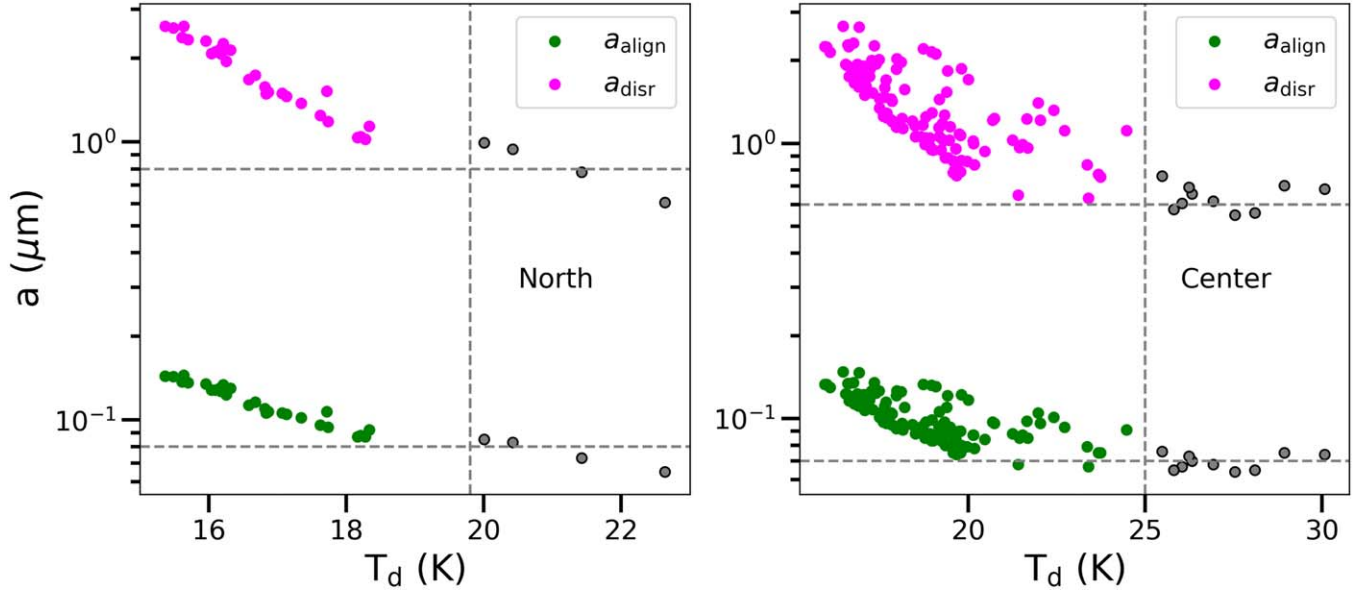


Figure 16. Grain size distributions for RAT-A and RAT-D mechanisms as a function of dust temperature in the North (left) and Center (right) regions. The gray points correspond to $T_d > 19.8$ K for the North region and $T_d > 25$ K for the Center region. The vertical gray dotted lines are drawn at $T_d = 19.8$ K and 25 K, which act as the transition temperatures (see Figure 7) and the horizontal lines are drawn at $a = 0.08 \mu\text{m}$ and $a = 0.8 \mu\text{m}$ for North, which indicate the median a_{align} and a_{disr} values for $T_d > 19.8$ K, respectively, and at $a = 0.07 \mu\text{m}$ and $a = 0.6 \mu\text{m}$ for the Center region for $T_d > 25$ K.

grains having embedded iron atoms as clusters. However, this high P value in the outer low-surface brightness regions may also be due to missing flux in these extended regions due to observing mode. For a study on this missing flux, please see the Appendix. The observed high P is also possible by the modern grain alignment theory that includes alignment by magnetic relaxation. Hence, we explore the effect of magnetic relaxation strength on the RAT-A efficiency of grains.

To describe the aligning effect of magnetic relaxation relative to the disalignment by gas collisions, a dimensionless parameter $\delta_{\text{mag,sp}}$, which gives the strength of the magnetic relaxation, was introduced (T. Hoang & A. Lazarian 2016) and is defined as the ratio of the gas collision damping timescale, τ_{gas} and the magnetic relaxation time, $\tau_{\text{mag,sp}}$. For super-paramagnetic grains having embedded iron clusters which are expected in dense regions because of grain evolution, the strength of magnetic relaxation is given by

$$\delta_{\text{mag,sp}} = \frac{\tau_{\text{gas}}}{\tau_{\text{mag,sp}}} = 56a_{-5}^{-1} \frac{N_{\text{cl}} \phi_{\text{sp,-2}} \hat{p}^2 B_3^2 k_{\text{sp}}(\Omega)}{\hat{\rho} n_4 T_{\text{gas},1}^{1/2} T_{\text{d},1}}, \quad (7)$$

where $a_{-5} = a/(10^{-5} \text{cm})$, $B_3 = B_{\text{tot}}/(10^3 \mu\text{G})$, and $n_4 = n_{\text{H}}/(10^4 \text{cm}^{-3})$ with $n_{\text{H}} \approx 2n(\text{H}_2)$ for molecular gas, $T_{\text{gas},1} = T_{\text{gas}}/(10 \text{K})$, $T_{\text{d},1} = T_{\text{d}}/(10 \text{K})$, and $\hat{p} = p/5.5$ with $p \approx 5.5$ the coefficient describing the magnetic moment of an iron atom, N_{cl} gives the number of iron atoms per cluster, ϕ_{sp} is the volume filling factor of iron clusters with $\phi_{\text{sp,-2}} = \phi_{\text{sp}}/0.01$ and $k_{\text{sp}}(\Omega)$ is the function of the grain rotation frequency Ω , which is of order unity (T. Hoang et al. 2022a).

Magnetic relaxation is considered effective for grain alignment when it happens much faster than the gas collision damping. The combined effect of suprathermal rotation of grains by RATs and magnetic relaxation can enhance the degree of RAT-A, which is known as the magnetically enhanced radiative torque (M-RAT) mechanism. Super-paramagnetic grains can achieve perfect alignment by the M-RAT

mechanism for $\delta_{\text{mag,sp}} > 10$ as derived from numerical calculations in T. Hoang & A. Lazarian (2016).

To study the effect of magnetic relaxation on the RAT-A efficiency in this filament, we calculate the $\delta_{\text{mag,sp}}$ values in all regions of the filament using Equation (7). We take the mean values of POS magnetic field strength B_{POS} for the North, Center, and South regions from A. Soam et al. (2019) and the values are $100 \pm 40 \mu\text{G}$, $470 \pm 190 \mu\text{G}$, and $60 \pm 34 \mu\text{G}$, respectively. The total magnetic field strength B_{tot} is 1.3 times the POS magnetic field strength B_{POS} as given in R. M. Crutcher et al. (2004). We calculate the B_{tot} values for each of the regions and using the values of other parameters, we calculate the $\delta_{\text{mag,sp}}$ values. We use $N_{\text{cl}} = 100$ and $\phi_{\text{sp}} = 0.01$ (about 3% of iron abundance as iron clusters, T. Hoang & A. Lazarian 2016). The maps of the strength of magnetic relaxation thus calculated and the polarization fraction are shown in Figure 17. In the North, the values of $\delta_{\text{mag,sp}}$ are in the range from 9 to 25 with a median value of 14.66, in the Center region the values are in the range from 35 to 590 with a median value of 293.09 and in the South from 5 to 9 with a median value of 6.32. It is found that the Center region has the strongest magnetic relaxation strength with $\delta_{\text{mag,sp}} \gg 10$. The North region also has $\delta_{\text{mag,sp}} > 10$. But the South region has $\delta_{\text{mag,sp}} < 10$. The magnetic field strengths are very large in the Center region followed by the North region and small in the South region (see Table 2). In the outer envelopes of the Center region, there are some pixels with very high magnetic relaxation strength and P values ranging from 8% to 20%. Also, in the North region, there are some pixels with $\delta_{\text{mag,sp}} > 10$ and P values more than 8%.

4. Discussion

In this section, we will discuss our results to explain the grain alignment and disruption mechanisms in different subregions of the filament with RAT-A and RAT-D.

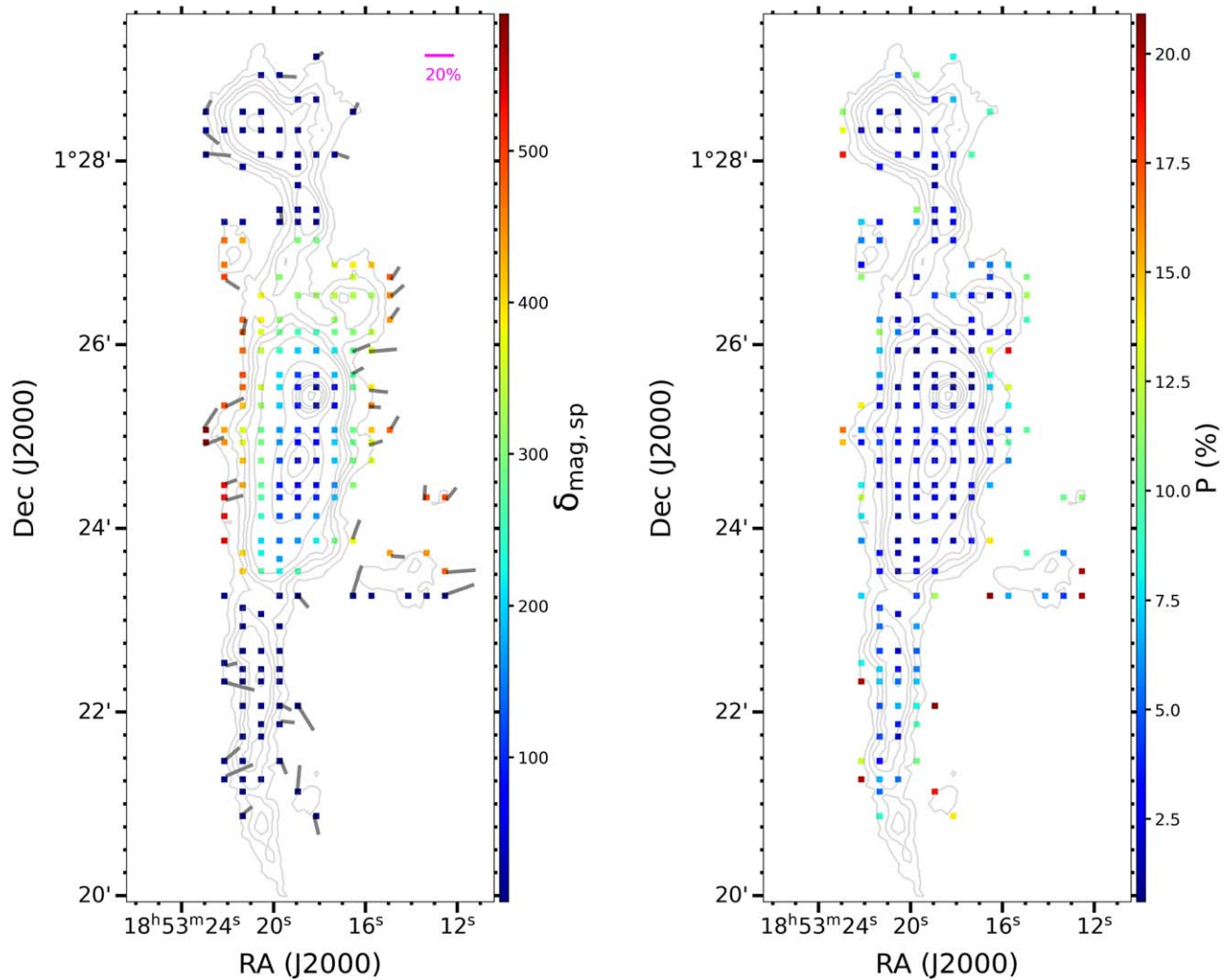


Figure 17. Maps of the strength of magnetic relaxation, $\delta_{\text{mag,sp}}$ (left panel) and polarization fraction P (right panel) in all regions of the G34 filament. The contours are the same as in Figure 2. The gray vectors denote P values ranging from 8% to 20%. A reference scale length of P value is also shown. In the outer parts of the filament, especially in the outer parts of the Center region, the values of $\delta_{\text{mag,sp}}$ are very high with some pixels showing P values from 8% to 20%.

4.1. Evidence for the RAT-A Mechanism

The decrease in the polarization fraction with the increase in gas column density $N(\text{H}_2)$ and total emission intensity I , called a polarization hole is found in many observational studies of dust polarization toward different environments (see, e.g., K. Pattle & L. Fissel 2019; T. Hoang et al. 2021). The real cause of the polarization hole is not yet clear. It can be caused by a decrease in grain alignment induced by RATs in denser regions with no embedded sources or by fluctuations in magnetic field orientations possibly induced by turbulence or both. In the G34 filament, which also harbors multiple cores in the North and Center regions, the polarization fraction decreases with increasing I and $N(\text{H}_2)$ (see Figures 5, 6). The North and South regions show overall steeper slopes compared to the Center region. However, the Center region has a steep slope of -0.54 ± 0.01 for $I < 850 \text{ mJy beam}^{-1}$, which is considered as the regions outside the cores. In our analysis, we find that the polarization fraction decreases with S in the South region and does not show an overall significant correlation with S in the North and Center regions (see Figure 8). Again, we find that the averaged grain alignment efficiency $P \times S$ decreases with increasing intensity (see Figure 9) in the North

and Center regions more similarly with the variation of polarization fraction with increasing intensity (see Figure 5) whereas it becomes nearly flat in the South region. A similar trend is also found in the variations of P and $P \times S$ with increasing $N(\text{H}_2)$ (see Figures 6, 11 (left panel), respectively). Therefore, the magnetic field tangling effect is more significant in the South and less significant in the North and Center regions. The decrease in the averaged grain alignment efficiency with increasing intensity can be explained by RAT-A theory.

Using RAT-A theory, we calculate the minimum size for aligned grains by RATs using the local physical parameters and obtained a map of alignment size (see Figure 12). We found that the value a_{align} is well correlated with the intensity (see Figure 13) in the North (up to $350 \text{ mJy beam}^{-1}$) and South regions, which means the alignment size increases in denser regions. But in the North region after an intensity of $350 \text{ mJy beam}^{-1}$, the alignment size decreases, which could be due to the presence of internal radiation from the MM3 core. Also, in the Center region, the alignment size increases up to around $850 \text{ mJy beam}^{-1}$ but decreases at higher intensity values, which could be due to the presence of internal radiation from cores MM1 and MM2. The increasing of alignment size

with intensity when no internal radiation source is present is an expectation of RAT-A theory. Also, there is anticorrelation in P with a_{align} and $P \times S$ with a_{align} for $I < 350 \text{ mJy beam}^{-1}$ (North region) and $I < 850 \text{ mJy beam}^{-1}$ (Center region), which are expected to be the regions outside the cores (see Figure 14). The decrease in grain alignment can majorly be due to a decrease in RAT-A efficiency in denser regions in the North region except the MM3 core and Center regions except for the MM1 and MM2 regions. For the South region, there is some effect of magnetic field fluctuations but the decrease in averaged alignment efficiency with a_{align} can be explained by RAT-A theory.

4.1.1. Correlation of Polarization Fraction with Dust Temperature

From RAT-A theory, it is expected that the polarization fraction P should increase with dust temperature T_d . The alignment size decreases with T_d and it will give a broader size distribution of aligned grains and larger polarization (H. Lee et al. 2020). We find that the North region shows an increase in P with T_d (see Figure 7) up to around 19.8 K and then decreases. Also, in the Center region, P increases with T_d up to around 19.8 K and then decreases. For the South region, P only increases with T_d . Also, $P \times S$ increases with T_d and then decreases after around 19.8 K as shown by the weighted running means in the North and Center regions but increases overall in the South region (see Figure 10). We know that the North and Center regions have embedded radiation sources and hence the governing radiation field in these regions is purely diffused ISRF outside MM1, MM2, and MM3 dense cores and is the combination of both the diffused ISRF and the local stellar radiation field in the regions of these dense cores. The South region does not have embedded sources and hence the dust temperature in this region is due to diffused ISRF. The increase in P with T_d in all the regions can be explained by RAT-A and the decrease in P can be a signature of RAT-D.

4.2. Implication for RAT-D Mechanism

As shown in Figure 7, we find the increase of P with increasing T_d up to nearly 19.8 K and then decreases in the North and Center regions (more significantly after 25 K in the Center region), which have embedded protostellar cores MM3 (North), MM1 and MM2 (Center). This decreasing of P at larger T_d values is opposite to the expectation of RAT-A theory (H. Lee et al. 2020). From the variation of averaged grain alignment efficiency $P \times S$ with T_d (see Figure 10) it is found that this variation almost nearly follows the variation of P with T_d (see Figure 7). The magnetic field tangling is less significant in causing the depolarization at higher T_d values in the high T_d core regions of the North and Center regions. Also, the median alignment and disruption sizes of grains when $T_d > 19.8 \text{ K}$ in the North region are nearly $0.08 \mu\text{m}$ and $0.86 \mu\text{m}$ and when $T_d > 25 \text{ K}$ in the Center region are nearly $0.07 \mu\text{m}$ and $0.64 \mu\text{m}$, respectively. It means that only the grains of sizes ranging from $0.08 \mu\text{m}$ to $0.86 \mu\text{m}$ can align in the North region of $T_d > 19.8 \text{ K}$ and only the grains of sizes ranging from $0.07 \mu\text{m}$ to $0.64 \mu\text{m}$ can align in the Center region of $T_d > 25 \text{ K}$. As shown in J. S. Mathis et al. (1977) the observational upper limit of the grain size distributions in the interstellar medium is $\approx 0.25 \mu\text{m}$. But in very dense star-forming regions, grain size is expected to increase due to grain growth. N. B. Ngoc et al. (2023) found the implications for grain growth in the G11.11-0.12 filament, which has gas volume density in the range from

10^3 to 10^5 cm^{-3} , with the lower limit of a_{max} greater than $0.3 \mu\text{m}$. We also expect that the actual size of most of the aligned grains may be far above the estimated a_{align} values in very dense regions of the filament with gas volume density in the range of 10^4 – 10^5 cm^{-3} as grain growth is expected in denser regions, thereby further narrowing the grain size distributions of grains that can be aligned. In the very dense and hot core regions of MM1, MM2, and MM3, we can expect a high upper limit of a_{max} values due to grain growth with the calculated a_{disr} values well below these a_{max} values. Whereas in the less dense and cold regions outside these cores, the a_{disr} values may be higher than the expected smaller upper limit of a_{max} values and hence no disruption of grains occurs in these regions. For a fixed upper limit of a_{max} , when RAT-D occurs larger grains are disrupted thereby removing grains from a_{max} to the disruption size a_{disr} which results in narrower grain size distribution of grain alignment and hence the polarization fraction gets reduced. The large grains which can be disrupted are the dominant contributors to the observed radiation at $850 \mu\text{m}$. Therefore, from our calculations of disruption sizes of grains and the observed decrease in polarization fraction in the North and Center regions at larger T_d values, we can imply the possibility of RAT-D occurring in these regions of the filament due to the presence of internal radiations from the hot and dense cores MM1, MM2 (Center) and MM3 (North). However, the depolarization with higher T_d values may also be caused by B -field tangling and/or change in the B -field inclination angle within the unresolved beam (T. Hoang & B. Truong 2024). But, there is a lack of details on the B -field tangling and inclination variation.

The evidence for the effect of RAT-D was also found in several studies in star-forming regions, e.g., Auriga (N. B. Ngoc et al. 2021), Oph A (L. N. Tram et al. 2021a), BN-KL region (L. N. Tram et al. 2021b; N. B. Ngoc et al. 2024), M17 (T. D. Hoang et al. 2022b).

4.3. Role of Magnetic Relaxation on RAT-A

The importance of enhanced magnetic relaxation combined with RATs to produce perfect grain alignment was first observationally estimated in G11.11-0.12 filament by N. B. Ngoc et al. (2023). In G34 filament, we find high values of polarization fraction mostly in the outer regions from around 8% to 20%. This value of P reaching nearly 20% is larger than the average value of the diffuse ISM with P nearly 15% observed by Planck Collaboration et al. (2020). Only RAT may not be able to produce this high value of P because of its dependence on parameters like grain shape, composition, and angle between the direction of the radiation field and the magnetic field (T. Hoang & A. Lazarian 2016; J. Herranen et al. 2021). These high P values in the outer low Stokes I regions may also be caused by missing flux in these regions due to the observation mode. This feature of high P in the outer low Stokes I regions is also observed in several studies using POL-2 and HAWC+ observations (e.g., J. Kwon et al. 2018; A. Soam et al. 2018; S. Coudé et al. 2019; K. Pattle et al. 2019; J.-W. Wang et al. 2019; D. Arzoumanian et al. 2021; N. B. Ngoc et al. 2023) and in the protostellar envelopes using ALMA observations (e.g., C. L. H. Hull et al. 2017; W. Kwon et al. 2019). However, the missing flux issue was not quantified and studied much. V. J. M. Le Gouellec et al. (2020) studied the statistical analysis of dust polarization properties in ALMA observations of class 0 protostellar cores and showed that the interferometric filtering may cause high polarization

fraction in the large-scale outer low Stokes I regions. However, N. Chau Giang et al. (2025) showed that the high polarization fraction in the outer protostellar envelope observed by ALMA is not entirely due to the interferometric filtering effect and could be produced by the thermal emission of aligned superparamagnetic grains with $N_{\text{cl}} \approx 10^2\text{--}10^3$ which can produce high intrinsic polarization fraction. Apart from the possible explanation due to missing flux, the observed high P is also possible according to the modern grain alignment theory, which incorporates the alignment by magnetic relaxation strength. The enhanced magnetic relaxation by grains having embedded iron inclusions can increase the RAT-A efficiency (T. Hoang & A. Lazarian 2016; T. Hoang et al. 2022a). In our estimation of the strength of magnetic relaxation, as shown in Figure 17, a small level of iron inclusions can produce $\delta_{\text{mag,sp}} \gg 10$, especially in the North and Center regions. The enhanced magnetic relaxation combined with RATs can increase the alignment of grains which may possibly explain the observed high polarization fraction in the outer parts of the North and Center regions of the G34 filament. Therefore, our results further support the possibility of an M-RAT alignment mechanism (T. Hoang & A. Lazarian 2016).

5. Conclusions

In this work, we use thermal dust polarization observations of the G34.43+0.24 filament at $850\ \mu\text{m}$ using POL-2 instrument mounted on JCMT to study dust grain alignment and disruption mechanisms over all the filament in three regions as North, Center, and South. Our main results are summarized as follows:

1. We find a decrease in the polarization fraction P with the increase in total intensity I and gas column density $N(\text{H}_2)$, the so-called polarization hole, in all the North, Center, and South regions of the filament. We also study the effect of magnetic field tangling on polarization holes by analyzing the polarization angle dispersion function. We find that P decreases as S increases in the South region, whereas it does not show any significant variations overall in the North and Center regions. In $P \times S$ variations with I and $N(\text{H}_2)$, the slope of the South region becomes shallower compared to $P-I$ and $P-N(\text{H}_2)$ variations, but the North and Center regions show a steep decrease in averaged grain alignment efficiency almost similar to $P-I$ and $P-N(\text{H}_2)$ variations. This suggests that the depolarization in the South region has a significant contribution from magnetic field fluctuations and for the North and Center regions, magnetic field tangling does not contribute much in causing depolarization. We find that the decrease in overall averaged grain alignment efficiency with an increase in total intensity and gas column density in all the regions can be explained by RAT-A theory except for the MM1, MM2 (Center), and MM3 (North) core regions.
2. To test whether the RAT mechanism can reproduce the observational data, we estimate the minimum grain alignment sizes, a_{align} for all the regions and the increase in a_{align} with increasing intensity in the North (up to $350\ \text{mJy beam}^{-1}$), Center (up to $850\ \text{mJy beam}^{-1}$), and South regions is in agreement with RAT-A theory. Also, from the analysis of P and $P \times S$ variation with a_{align} , we find that the effect of magnetic field tangling is significant

to cause depolarization in the South region and not very significant in the North and Center regions. The depolarizations in the North and Center regions are mainly due to the decrease in the net alignment efficiency of grains. The decrease in P and $P \times S$ with a_{align} for the regions except the MM1, MM2 (Center) and MM3 (North) core regions can be explained by RAT-A theory.

3. We find hints of the RAT-D effect in the North (MM3) and Center (MM1 and MM2) regions from the analysis of P variation with T_{d} and the calculation of minimum alignment and disruption sizes of grains. The variation of P with T_{d} is found to be almost similar to the variation of $P \times S$ with T_{d} in the North and Center regions. Our study finds that the decrease in P at large T_{d} values in the North and Center regions can be associated with the regions of the dense and hot protostellar cores MM1, MM2 (Center) and MM3 (North). We find potential evidence for the possible explanation of this observed feature in the core regions by the RAT-D mechanism due to the presence of high-luminosity internal radiations from the protostellar cores, although the B -field tangling and B -field inclination angle variations within the unresolved beam can also contribute to the decrease in the polarization fraction.
4. We also study the importance of enhanced magnetic relaxation on RAT-A efficiency and find a possible scenario in which the M-RAT alignment mechanism could potentially explain the observed high polarization fraction of 8%–20% in the outer protostellar envelopes of the North and Center regions of the filament in the context of modern grain alignment theory. The high polarization fraction could also possibly be caused by any missing flux, if present, in the outer low Stokes I regions.

In the future, we will do a pixel-by-pixel polarization modeling of this G34 region using *DustPol* and compare it with the observational results.

Acknowledgments

The authors greatly thank the anonymous reviewer for a detailed review and providing a very constructive report that considerably helped in improving the clarity of the manuscript. This work was partly supported by a grant from the Simons Foundation to IFIRSE, ICISE (916424, N.H.). We would like to thank the ICISE staff for their enthusiastic support. T.H acknowledges the support from the main research project (No. 2025186902) from Korea Astronomy and Space Science Institute (KASI). P.N.D and N.B.N were funded by Vingroup Innovation Foundation (VINIF) under project code VINIF.2023.DA.057. This research has made use of observational data from the JCMT POL-2 instrument. JCMT is operated by the East Asian Observatory on behalf of the National Astronomical Observatory of Japan; Academia Sinica Institute of Astronomy and Astrophysics; the Korea Astronomy and Space Science Institute; the Operation, Maintenance and Upgrading Fund for Astronomical Telescopes and Facility Instruments, budgeted from the Ministry of Finance of China and administrated by the Chinese Academy of Sciences and, the National Key R&D Program of China.

Facilities: JCMT, Herschel Space Observatory.

Software: Astropy (Astropy Collaboration et al. 2013, 2018), SciPy (P. Virtanen et al. 2020).

Appendix Synthetic Intensity Map

There may be missing flux in the outer Stokes I low-surface brightness regions of the filament, which may produce a high polarization fraction. To check the expected flux in these outer regions, we compute the synthetic $850\ \mu\text{m}$ intensity map using Herschel PACS/SPIRE data at 70, 160, 250, 350, and $500\ \mu\text{m}$. The process of estimating the synthetic map is described as follows. First, all the Herschel data at different wavelengths and resolutions are convolved to Herschel $500\ \mu\text{m}$ FWHM beam size of $35''$ and reprojected on the same grid of the observed JCMT $850\ \mu\text{m}$. We use the following modified blackbody function (J. Kauffmann et al. 2008) for the spectral energy distribution fitting in each pixel position,

$$I_\nu = B_\nu(T_d)(1 - e^{-\tau_\nu}), \quad (\text{A1})$$

$$B_\nu(T_d) = \frac{2h\nu^3}{c^2} \frac{1}{e^{h\nu/k_B T_d} - 1}, \quad (\text{A2})$$

$$\tau_\nu = \mu_{\text{H}_2} m_{\text{H}} \kappa_\nu N(\text{H}_2), \quad (\text{A3})$$

where $B_\nu(T_d)$ is the Planck function at the dust temperature T_d , τ_ν the optical depth, μ_{H_2} the mean molecular weight per hydrogen molecule, m_{H} is the hydrogen atom mass, κ_ν is the dust opacity and $N(\text{H}_2)$ the H_2 column density. We use $\mu_{\text{H}_2} = 2.8$. We use κ_ν values of 1.76, 0.4, 0.195, 0.1, and $0.05\ \text{cm}^2\ \text{g}^{-1}$ (V. Ossenkopf & T. Henning 1994) considering a dust-to-gas ratio of 0.01 for 70, 160, 250, 350 and $500\ \mu\text{m}$, respectively. The best-fitted parameters T_d and $N(\text{H}_2)$ are derived for each pixel. Then, we use these fitted parameters in the following equation to derive the

synthetic $850\ \mu\text{m}$ intensity map:

$$I_{850} = B_{850}(T_d)(1 - e^{-\tau_{850}}). \quad (\text{A4})$$

We use the dust opacity at $850\ \mu\text{m}$, κ_{850} value of $0.0197\ \text{cm}^2\ \text{g}^{-1}$ (V. Ossenkopf & T. Henning 1994). The synthetic map thus derived is compared with the observed JCMT/POL-2 $850\ \mu\text{m}$ intensity map convolved to the resolution of SPIRE $500\ \mu\text{m}$. We perform a further scaling of the synthetic map to match it with the observed intensity by a best-fit scaling factor. The JCMT/POL-2 observed and synthetic $850\ \mu\text{m}$ maps (convolved to SPIRE $500\ \mu\text{m}$ resolution of $35''$) are shown in the left and right panels of Figure 18. Then we compare both the intensities as shown in Figure 19 (right upper panel). For the intensity values below $100\ \text{MJy}\ \text{sr}^{-1}$, it seems to be well correlated with some deviations. However, there are many deviations at higher intensity values. We also compute the differences between the synthetic and observed intensities for the outer low-surface brightness regions having polarization fractions in the range from 8% to 20% and the map of these differences is shown in Figure 19 (left panel). We find that some regions have somewhat larger differences and some regions have small differences. A comparison of the observed and the synthetic intensities for the outer regions is also shown in Figure 19 (right lower panel) with the color bar denoting the difference values. The synthetic intensity map may not be exactly similar to the observed intensity map. Since the intensities have significant deviations in the bright, high-intensity regions, the expected differences in the outer regions stand only as an approximation, which still lacks an accurate comparison to find any missing flux in these outer regions. However, we expect the possibility of having missing flux in the large-scale outer low Stokes I regions.

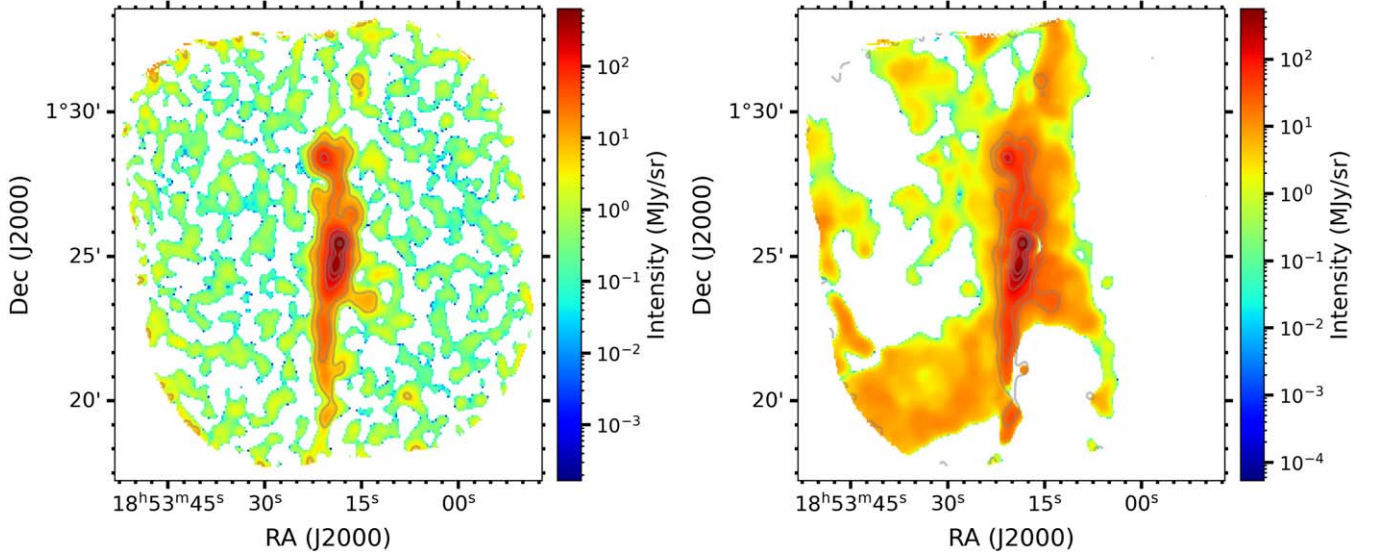


Figure 18. Maps of JCMT/POL-2 observed (left) and synthetic (right) $850\ \mu\text{m}$ intensities. The contours are drawn at I values of 5, 20, 100, 200, 300, $600\ \text{MJy}\ \text{sr}^{-1}$ in both maps. Both maps are at SPIRE $500\ \mu\text{m}$ resolution of $35''$.

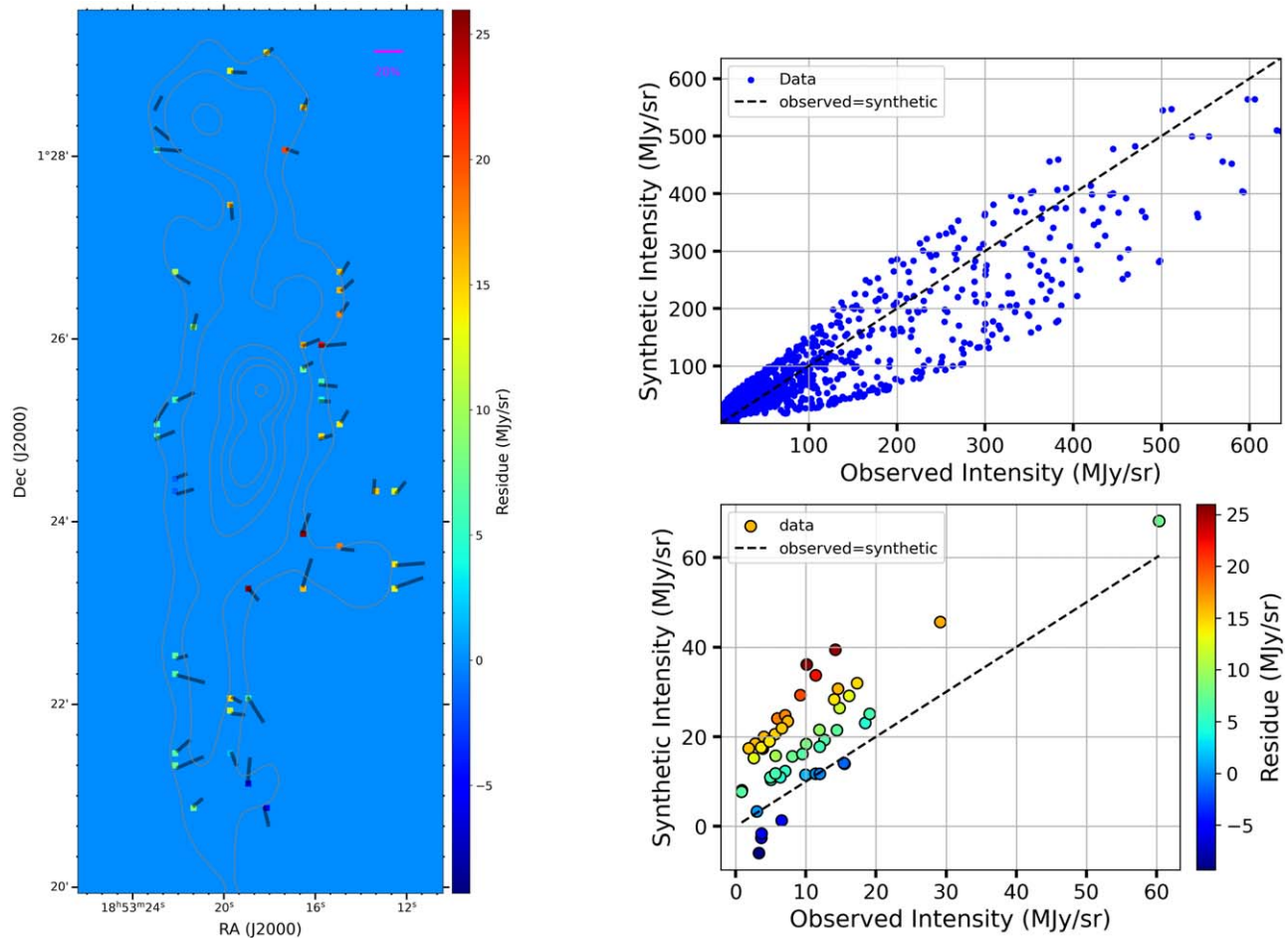


Figure 19. Map of distribution of residual intensity between the synthetic and observed $850\ \mu\text{m}$ intensities for the outer regions of the filament (left panel). The gray vectors denote P values ranging from 8% to 20%. A reference scale of P is also shown. Right upper panel shows comparison between the observed and synthetic intensities with the dashed black line denoting the equality of both. The right lower panel shows the comparison between the observed and the synthetic intensities only for the outer regions, as shown in the left panel with the color bar denoting the residual intensity values and the dashed black line denoting the equality of both the observed and synthetic intensities.

ORCID iDs

Saikhom Pravash <https://orcid.org/0009-0002-6171-9740>
 Archana Soam <https://orcid.org/0000-0002-6386-2906>
 Pham Ngoc Diep <https://orcid.org/0000-0002-2808-0888>
 Thiem Hoang <https://orcid.org/0000-0003-2017-0982>
 Nguyen Bich Ngoc <https://orcid.org/0000-0002-5913-5554>
 Le Ngoc Tram <https://orcid.org/0000-0002-6488-8227>

References

Adam, R., Adane, A., Ade, P. A. R., et al. 2018, *A&A*, 609, A115
 Alina, D., Montier, L., Ristorcelli, I., et al. 2016, *A&A*, 595, A57
 Andersson, B. G., Lazarian, A., & Vaillancourt, J. E. 2015, *ARA&A*, 53, 501
 Arzoumanian, D., Furuya, R. S., Hasegawa, T., et al. 2021, *A&A*, 647, A78
 Astropy Collaboration, Price-Whelan, A. M., Sipőcz, B. M., et al. 2018, *AJ*, 156, 123
 Astropy Collaboration, Robitaille, T. P., Tollerud, E. J., et al. 2013, *A&A*, 558, A33
 Bethell, T. J., Chepurnov, A., Lazarian, A., & Kim, J. 2007, *ApJ*, 663, 1055
 Chau Giang, N., Le Gouellec, V. J. M., Hoang, T., Maury, A. J., & Hennebelle, P. 2025, *ApJ*, 980, 105
 Chen, H.-R., Liu, S.-Y., Su, Y.-N., & Wang, M.-Y. 2011, *ApJ*, 743, 196
 Coudé, S., Bastien, P., Houde, M., et al. 2019, *ApJ*, 877, 88
 Crutcher, R. M. 2012, *ARA&A*, 50, 29
 Crutcher, R. M., Nutter, D. J., Ward-Thompson, D., & Kirk, J. M. 2004, *ApJ*, 600, 279
 Davis, L. J., & Greenstein, J. L. 1951, *ApJ*, 114, 206

Dolginov, A. Z., & Mitrofanov, I. G. 1976, *Ap&SS*, 43, 291
 Draine, B. T. 2003, *ARA&A*, 41, 241
 Draine, B. T. 2011, *Physics of the Interstellar and Intergalactic Medium* (Princeton, NJ: Princeton Univ. Press)
 Draine, B. T., & Hensley, B. S. 2021, *ApJ*, 919, 65
 Draine, B. T., & Weingartner, J. C. 1997, *ApJ*, 480, 633
 Falceta-Gonçalves, D., Lazarian, A., & Kowal, G. 2008, *ApJ*, 679, 537
 Foster, J. B., Arce, H. G., Kassis, M., et al. 2014, *ApJ*, 791, 108
 Friberg, P., Bastien, P., Berry, D., et al. 2016, *Proc. SPIE*, 9914, 991403
 Hall, J. S. 1949, *Sci*, 109, 166
 Harper, D. A., Runyan, M. C., Dowell, C. D., et al. 2018, *JAI*, 7, 1840008
 Herranen, J., Lazarian, A., & Hoang, T. 2021, *ApJ*, 913, 63
 Hildebrand, R. H. 1988, *QJRAS*, 29, 327
 Hiltner, W. A. 1949, *ApJ*, 109, 471
 Hoang, T., & Lazarian, A. 2008, *MNRAS*, 388, 117
 Hoang, T., & Lazarian, A. 2014, *MNRAS*, 438, 680
 Hoang, T., & Lazarian, A. 2016, *ApJ*, 831, 159
 Hoang, T., Tram, L. N., Lee, H., & Ahn, S.-H. 2019, *NatAs*, 3, 766
 Hoang, T., Tram, L. N., Lee, H., Diep, P. N., & Ngoc, N. B. 2021, *ApJ*, 908, 218
 Hoang, T., Tram, L. N., Minh Phan, V. H., et al. 2022a, *AJ*, 164, 248
 Hoang, T., & Truong, B. 2024, *ApJ*, 965, 183
 Hoang, T. D., Ngoc, N. B., Diep, P. N., et al. 2022b, *ApJ*, 929, 27
 Chou, C. L. H., Girart, J. M., Tychoniec, Ł., et al. 2017, *ApJ*, 847, 92
 Hull, C. L. H., Plambeck, R. L., Kwon, W., et al. 2014, *ApJS*, 213, 13
 Jones, T. J. 1989, *ApJ*, 346, 728
 Jones, T. J., Klebe, D., & Dickey, J. M. 1992, *ApJ*, 389, 602
 Kauffmann, J., Bertoldi, F., Bourke, T. L., Evans, N. J., II, & Lee, C. W. 2008, *A&A*, 487, 993
 Kwon, J., Doi, Y., Tamura, M., et al. 2018, *ApJ*, 859, 4

- Kwon, W., Stephens, I. W., Tobin, J. J., et al. 2019, *ApJ*, 879, 25
- Lazarian, A. 2007, *JQSRT*, 106, 225
- Lazarian, A., Andersson, B. G., & Hoang, T. 2015, in *Polarimetry of Stars and Planetary Systems*, ed. L. Kolokolova, J. Hough, & A.-C. Levasseur-Regourd, 81 (Cambridge: Cambridge Univ. Press)
- Lazarian, A., & Hoang, T. 2007, *MNRAS*, 378, 910
- Le Gouellec, V. J. M., Maury, A. J., Guillet, V., et al. 2020, *A&A*, 644, A11
- Lee, H., Hoang, T., Le, N., & Cho, J. 2020, *ApJ*, 896, 44
- Mathis, J. S., Rumpl, W., & Nordsieck, K. H. 1977, *ApJ*, 217, 425
- Molinari, S., Brand, J., Cesaroni, R., Palla, F., & Palumbo, G. G. C. 1998, *A&A*, 336, 339
- Ngoc, N. B., Diep, P. N., Hoang, T., et al. 2023, *ApJ*, 953, 66
- Ngoc, N. B., Diep, P. N., Parsons, H., et al. 2021, *ApJ*, 908, 10
- Ngoc, N. B., Hoang, T., Diep, P. N., & Tram, L. N. 2024, *ApJ*, 974, 118
- Ossenkopf, V., & Henning, T. 1994, *A&A*, 291, 943
- Pan, S., Liu, H.-L., & Qin, S.-L. 2024, *ApJ*, 960, 76
- Panopoulou, G. V., Clark, S. E., Hacar, A., et al. 2022, *A&A*, 657, L13
- Pattle, K., & Fissel, L. 2019, *FrASS*, 6, 15
- Pattle, K., Lai, S.-P., Hasegawa, T., et al. 2019, *ApJ*, 880, 27
- Planck Collaboration, Aghanim, N., Akrami, Y., et al. 2020, *A&A*, 641, A12
- Rathborne, J. M., Garay, G., Jackson, J. M., et al. 2011, *ApJ*, 741, 120
- Rathborne, J. M., Jackson, J. M., Chambers, E. T., et al. 2010, *ApJ*, 715, 310
- Rathborne, J. M., Jackson, J. M., & Simon, R. 2006, *ApJ*, 641, 389
- Rathborne, J. M., Jackson, J. M., Zhang, Q., & Simon, R. 2008, *ApJ*, 689, 1141
- Sakai, T., Sakai, N., Furuya, K., et al. 2015, *ApJ*, 803, 70
- Sakai, T., Yanagida, T., Furuya, K., et al. 2018, *ApJ*, 857, 35
- Sanhueza, P., Jackson, J. M., Foster, J. B., et al. 2012, *ApJ*, 756, 60
- Santos, F. P., Chuss, D. T., Dowell, C. D., et al. 2019, *ApJ*, 882, 113
- Shepherd, D. S., Nürnbergger, D. E. A., & Bronfman, L. 2004, *ApJ*, 602, 850
- Shepherd, D. S., Povich, M. S., Whitney, B. A., et al. 2007, *ApJ*, 669, 464
- Soam, A., Liu, T., Andersson, B. G., et al. 2019, *ApJ*, 883, 95
- Soam, A., Pattle, K., Ward-Thompson, D., et al. 2018, *ApJ*, 861, 65
- Tatsuuma, M., Kataoka, A., & Tanaka, H. 2019, *ApJ*, 874, 159
- Tram, L. N., & Hoang, T. 2022, *FrASS*, 9, 923927
- Tram, L. N., Hoang, T., Lee, H., et al. 2021a, *ApJ*, 906, 115
- Tram, L. N., Hoang, T., Wiesemeyer, H., et al. 2024, *A&A*, 689, A290
- Tram, L. N., Lee, H., Hoang, T., et al. 2021b, *ApJ*, 908, 159
- Truong, B., & Hoang, T. 2024, arXiv:2407.14896
- Virtanen, P., Gommers, R., Oliphant, T. E., et al. 2020, *NatMe*, 17, 261
- Wang, J.-W., Lai, S.-P., Eswaraiah, C., et al. 2019, *ApJ*, 876, 42
- Wootten, A., & Thompson, A. R. 2009, *IEEEP*, 97, 1463
- Yanagida, T., Sakai, T., Hirota, T., et al. 2014, *ApJL*, 794, L10
- Zhang, Q., Qiu, K., Girart, J. M., et al. 2014, *ApJ*, 792, 116
- Zucker, C., & Chen, H. H.-H. 2018, *ApJ*, 864, 152